Energy 313 (2024) 134164

Contents lists available at ScienceDirect

Energy

journal homepage: www.elsevier.com/locate/energy

Efficient design of a hybrid power system incorporating resource variability

Juan M. Lujano-Rojas [*], Rodolfo Dufo-López, Jesús Sergio Artal-Sevil, Eduardo García-Paricio

Department of Electrical Engineering, University of Zaragoza, Calle María de Luna 3, 50018, Zaragoza, Spain

ARTICLE INFO

Handling Editor: Neven Duic

Keywords:
Hybrid power system
Genghis Khan shark optimizer
Genetic algorithm
Optimization
Lead-acid battery

ABSTRACT

The optimal design of small-scale energy systems is a critical step in rural electrification projects, offering valuable insights for integrating renewable energy sources on a broader scale. This paper analyzes the sizing of isolated energy systems using the Genghis Khan Shark Optimizer, taking into account the variability of wind and solar resources across diverse scenario groups to enhance computational efficiency. Specifically, three scenario sets were utilized: training, validation, and testing. The training set was applied to assess the objective function across all optimization agents, while the validation set was used to independently evaluate the performance of the agent with the highest fitness score. Finally, the testing set was employed to verify the performance of the accepted solution. By selecting a limited number of scenarios for the training set and a moderate number for the validation and testing sets, we reduced the computational load associated with analyzing the entire population, allowing for greater focus on the most promising agent identified at each iteration. Results from a case study revealed that the proposed method identified an energy system configuration 8.05 % better than the configuration obtained using a genetic algorithm.

1. Introduction

Access to energy in remote areas is crucial for supporting social and economic development, as it enables the operation of essential services such as schools and healthcare facilities. In these settings, power can be provided through fossil fuel-powered generators (e.g., diesel or gasoline) or by incorporating renewable sources, such as wind and solar energy, in combination with a battery energy storage system (BESS), thereby creating a hybrid power system (HPS).

Determining the optimal sizing for each energy source presents a complex challenge, given the extensive variety of generators, photovoltaic (PV) panels, wind turbines (WTs), and BESS units available from different manufacturers. The process of selecting an ideal configuration for a specific location is a combinatorial problem, requiring equipment choices from multiple manufacturers to minimize costs and reduce the system's environmental impact over its lifespan. The vast number of potential combinations poses significant computational demands, making heuristic optimization techniques (HOTs) a preferred solution for scientists and engineers working on this challenge.

HPS design can aim to minimize either the total net present cost (TNPC) alone or both TNPC and greenhouse gas (GHG) emissions. For TNPC minimization, a mono-objective optimization (MoOO) approach is employed. In contrast, a multi-objective optimization (MuOO) algorithm is used when both TNPC and GHG emissions are considered. In MoOO, the system design is based on estimated TNPC, while in MuOO, decision-makers select the most suitable configuration from the Pareto front, highlighting a fundamental distinction in heuristic methodologies between MoOO and MuOO. In the following sub-sections, we present recent studies in the field of HPS sizing utilizing MoOO and MuOO approaches.

1.1. Multi-objective optimization for hybrid power system design

For HPS sizing with MoOO, commonly applied algorithms include genetic algorithms (GAs), particle swarm optimization (PSO), simulated annealing (SA), and differential evolution (DE), with ongoing research focused on refining and enhancing these methods. For example, Sadeghibakhtiar et al. [1] applied a GA to design a PV/WT/BESS residential HPS in Italy, accounting for uncertainties in wind and solar resources through Monte Carlo simulations (MCSs). Their optimization aimed to minimize TNPC while maintaining system reliability, as measured by the loss of load probability (LOLP). This study achieved a TNPC of €75795 for a system with 95 % reliability. Chen and Zhang [2] applied modified PSO and SA methods to design an HPS comprising PV panels, a diesel generator (DG), and a BESS for a remote area in China. The modified PSO effectively minimized TNPC. Then, the authors conducted

---

* Corresponding author.
E-mail addresses: lujano.juan@unizar.es (J.M. Lujano-Rojas), rdufo@unizar.es (R. Dufo-López), egarciap@unizar.es (E. García-Paricio).

https://doi.org/10.1016/j.energy.2024.134164
Received 17 August 2024; Received in revised form 8 November 2024; Accepted 7 December 2024
Available online 9 December 2024
0360-5442/© 2024 The Authors. Published by Elsevier Ltd. This is an open access article under the CC BY license (http://creativecommons.org/licenses/by/4.0/).

Table 1
Key features of recent research on HPS management and design by MoOO.

Reference	Algorithm	Methodology
Sadeghibakhtiar et al. [1]	GA	It considers both resource variability and system reliability; however, the BESS model does not account for degradation over its lifetime.
Chen and Zhang [2]	PSO and SA	It mitigates stagnation around a local optimum by performing 30 independent optimizations. However, uncertainty regarding renewable resources is not considered, nor is the reduction in BESS lifespan incorporated.
Kamal et al. [3]	DE, PSO, and GA	DE achieved the optimal configuration among the benchmark methods.
Araoye et al. [4]	GOA and HOMER Pro®	Through sensitivity analysis, the researchers incorporate variations in renewable resources and other techno-economic parameters, as well as their effects on the TNPC. However, the impact of BESS performance and replacement timing could also be integrated into the sensitivity analysis.
Abdelsattar et al. [5]	DO	It combines the COE, LOLP, and GHG emissions into a single objective to achieve improved results from multiple perspectives. However, the capacity degradation of the BESS due to cycling is not modeled, nor is its impact on the TNPC.
Amoussou et al. [6]	COA, WOA, SCA, and GOA	The authors assessed the impact of LOLP on the optimal configuration through sensitivity analysis. However, the BESS model does not allow for estimation of the impact of its replacement on the TNPC.
Bakeer et al. [7]	AVOA, GOA, GPC, and HOMER Pro®	The researchers independently repeated the optimization process 20 times to identify the global optimum. Nevertheless, the reduction in BESS operational time due to wear is not accounted for.
Bouaouda and Sayouti [8]	QBWO, BWO, PSO, and CSA	The authors performed a sensitivity analysis on load demand and the availability of each system component. Additionally, QBWO demonstrates an accelerated convergence rate.
Farh [9]	RLNNA, GA, PSO, MRFO, and SDO	The authors conducted 50 optimization experiments to find the global optimum, subsequently evaluating the algorithm's performance using the mean, standard deviation, and the highest and lowest costs. However, the BESS model is linear and does not include any method for estimating the BESS replacement time.
Jahangir et al. [10]	Complementarity of natural resources and HOMER Pro®	Analyzing the complementarity of natural resources offers a rapid solution comparable to those derived from more complex simulation models, such as HOMER Pro® software. Additionally, solar resource uncertainty has been incorporated. However, the reduction in BESS lifespan due to discharging conditions has not been included.
Jiang et al. [11]	SDP	This approach considers the uncertainty of renewable power, thereby enhancing the operational robustness of the HPS.
Yang et al. [12]	TLBO-CSA	It incorporates the uncertainty of clean energy sources and optimizes the management of DR resources.

sensitivity analyses on fuel and CO_2 prices, with cost of energy (COE) values ranging from \$0.28 to \$0.64/kWh. Kamal et al. [3] developed a DE-based model to design an HPS in India, using PV panels, a biogas generator (BG), WTs, a DG, and a BESS, achieving a COE of \$0.22/kWh, representing improvements of 4.3 % and 5.2 % over PSO and GA, respectively.

Researchers continue to develop new HOTs for MoOO to assist engineers and practitioners in designing cost-effective, high-performance HPS. In this regard, Araoye et al. [4] applied the grasshopper optimization algorithm (GOA) to size an HPS in Nigeria, incorporating PV panels, WTs, BG, DG, BESS, and a hydropower (HP) generator. GOA, inspired by the hunting and swarming behavior of grasshoppers, demonstrated superior results compared to the updated HOMER Pro® software, achieving a COE of \$0.01783/kWh, significantly influenced by the BG.

For an Egyptian system, Abdelsattar et al. [5] explored various configurations using PV modules, WTs, BESS, and DG, optimized through the dandelion optimizer (DO), inspired by the dispersal behavior of dandelion seeds. By balancing COE, LOLP, and GHG emissions, the study reported COE values between \$0.2311 and \$0.3282/kWh, depending on the inclusion of wind generation.

Amoussou et al. [6] employed the crayfish optimization algorithm (COA) to size an HPS in Cameroon, inspired by crayfish foraging behavior. COA outperformed other algorithms such as the whale optimization algorithm (WOA), sine cosine algorithm (SCA), and GOA in COE by margins of 0.06 %, 0.122 %, and 0.39 %, respectively, depending on the architecture.

Bakeer et al. [7] utilized the African vultures optimization approach (AVOA) for an HPS in Egypt, comprising PV panels, WTs, DG, and BESS. AVOA outperformed HOMER Pro®, GOA, and the Giza pyramid construction (GPC) algorithm, achieving a COE of \$0.0947/kWh with superior convergence and computation time across 20 trials.

Bouaouda and Sayouti [8] applied quantum beluga whale optimization (QBWO) in Morocco, combining beluga whale optimization (BWO) with quantum mechanics for enhanced performance, achieving a COE of \$0.264/kWh with a 4.6 % LOLP, surpassing BWO, PSO, and CSA.

Farh [9] used a reinforcement learning neural network algorithm (RLNNA) for HPS design in Saudi Arabia, including PV modules, WTs, DG, and BESS. RLNNA demonstrated efficient, rapid convergence compared to other algorithms like GA, PSO, and manta ray foraging optimization (MRFO).

Jahangir et al. [10] proposed a methodology leveraging resource complementarity for an HPS in Canada, the UK, and Pakistan, analyzing resource variability over critical months with results consistent with HOMER Pro®. Specifically, the design derived from the resource complementarity analysis, compared to that recommended by HOMER Pro®, features a PV generator that is 57 % smaller and a BESS that is 39 % larger.

In rural electrification, HPSs are typically managed using a load-following strategy, in which renewable generation and BESS are prioritized, and DG is used to meet the remaining load demand. Conversely, in higher-capacity HPS, daily forecasting of renewable generation is conducted to improve clean power integration. In this context, Jiang et al. [11] introduced a sizing method based on stochastic optimization, performing a long-term analysis to estimate the optimal operating strategy through stochastic dynamic programming (SDP).

Yang et al. [12] developed a model implemented in two layers to manage systems equipped with renewable and demand response (DR) resources. First, the uncertainty of renewable generation is represented through a scenario generation and reduction approach. Then, the upper layer minimizes DR-related costs, while the lower layer minimizes overall expenses. The optimization task is conducted using a combination of the teaching-learning based optimization (TLBO) and CSA, with results highlighting the effectiveness of the proposed method for HPS management.

Table 1 presents a summary of each aforementioned MoOO technique, highlighting their general capabilities and limitations in a compact format.

1.2. Multi-objective optimization for hybrid power system design

To enhance the environmental benefits of HPS, scientists have made significant efforts to improve existing MuOO techniques and develop new ones, enabling practitioners to design HPSs that balance TNPC and GHG emissions. Commonly used methods include the non-dominated sorting genetic algorithm version II (NSGA-II) and multi-objective particle swarm optimization (MOPSO). For instance, Sadeghibakhtiar et al. [1] employed NSGA-II in combination with the technique for order preference by similarity to an ideal solution (TOPSIS).

Cheraghi and Jahangir [13] implemented a design tool based on NSGA-II and MOPSO, incorporating PV panels, WTs, a ground source heat pump, a DG, a BESS, and an FC. This model optimizes COE, GHG emissions, and the human development index (HDI) simultaneously to provide enriched data for decision-making. The results showed that GHG emissions could be reduced by at least 46 % compared to a coal-based generation unit and by at least 3 % compared to a unit powered by natural gas.

Ansari [14] proposed a technique based on NSGA-II for designing an HPS with a PV generator, a DG, and an FC, with LOLP and TNPC as the main objectives. Pareto front results were then analyzed using the analytic hierarchy process (AHP) combined with TOPSIS. Demonstrating this approach in Iran, the author conducted sensitivity analysis and found that a 50 % reduction in FC reduced TNPC by 8.93 %, while a 50 % increase in fuel cost raised TNPC by 24.55 %. Additionally, researchers estimated that TNPC could increase by 30.50 % due to uncertainties in natural resources.

Liu et al. [15] presented a sizing tool for an HPS incorporating a concentrating solar power (CSP) device, a thermal energy storage system, PV modules, WTs, a BESS, and electric heaters. The researchers analyzed local consumption, sales, and virtual power plant (VPP) modes, each under scenarios of load demand and electricity price uncertainty. The MuOO model addresses factors related to LOLP, COE, and net economic benefit for sales and VPP modes only, using NSGA-II and TOPSIS. Analyzing an HPS in China, the authors observed that PV panel quantity and BESS size, along with CSP—providing 31–38 % of total power—were critical to performance. Incorporating electric heaters allowed for the utilization of excess electricity, enhancing overall system performance.

The HPS management problem can be formulated using MuOO to minimize operational costs and environmental impact concurrently. Following this research direction, Ahmed et al. [16] addressed hydro-thermal coordination with MuOO, including uncertainties in wind and solar generation. The authors used the adaptive salp swarm algorithm (ASSA) for optimization and combined RETScreen® software with the point estimation approach to model solar and wind generation. In a case study, the approach demonstrated reductions of 10 % in operating costs and 64 % in GHG emissions.

Belbachír et al. [17] presented a MoOO methodology created by summing independent objectives, thus transforming a MuOO into a MoOO. This technique is used for BESS sizing and placement, considering characteristics of distribution systems (DSs) such as power losses (PLs) and voltage deviations (VDs). The authors proposed an improvement to the artificial hummingbird algorithm (AHA), inspired by hummingbird flight behavior, by incorporating long-term memory. The resulting algorithm, the long-term memory artificial hummingbird algorithm (LMAHA), demonstrated better performance than AHA and other algorithms, including gradient-based optimizer (GBO), artificial rabbits optimization (ARO), pelican optimization algorithm (POA), PSO, GA, and DE. Across two test DSs, the study observed reductions in daily PL by 72–82 % and in daily VD by 56–67 %.

Mbasso et al. [18] combined MOPSO and the multi-objective grey wolf optimizer (MOGWO) to leverage the strengths of both techniques, improving optimization outcomes. The MuOO implementation using the MOPSO-MOGWO algorithm was applied to design a PV/BESS system in Cameroon, minimizing LOLP and maximizing HPS autonomy, including BESS energy. Considering different load profiles based on environmental conditions, the researchers noted that the combined MOPSO-MOGWO algorithm outperformed individual implementations.

Hai et al. [19] developed a management model for a smart parking lot with PV generation, an FC, and DR resources. This technique combines WOA and pattern search (PS) to address average and deviation costs from a MuOO perspective. The method employs fuzzy theory to select appropriate solutions from the Pareto front, accounting for the negative impact of uncertainty on HPS performance. Comparisons with CSA and TLBO highlighted the technique's promise, showing a reduction in uncertainty of approximately 41 %.

Alahmad et al. [20,21] proposed a design model using NSGA-II and MOPSO. Uncertainty was incorporated through MCSs, combining scenario generation and reduction techniques with probabilistic load flow (PLF) studies. Technical constraints of DS were considered, establishing optimization goals related to operating costs, PL, and VD. The authors examined BESS and compressed air energy storage system (CAES) technologies, showing that dependency on DS or thermal generation units decreased by 15–31 %, along with reductions in PLs and improvements in voltage profiles.

Pandya et al. [22] focused on solving the optimal power flow (OPF) problem with considerations for renewable generation uncertainty and the effects of the flexible AC transmission system (FACTS). Location and capacity of FACTS equipment were optimized using the multi-objective moth flame optimizer (MOMFO), inspired by moth navigation. In another study [23], OPF for an HPS with a PV farm, WTs, and HP generation was solved using the multi-objective RIME (MORIME) algorithm, inspired by rime-ice behavior. This approach outperformed multi-objective versions of WOA, GWO, and MRFO.

Agrawal et al. [24] employed the multi-objective thermal exchange optimization (MOTEO) algorithm to solve the OPF problem under uncertainty. MOTEO, based on Newton's law of cooling, optimized an HPS with PV modules, WTs, a small HP unit, a DG, and the DS, incorporating VDs and PLs minimization. The authors demonstrated MOTEO's effectiveness by comparing it with multi-objective versions of WOA and GWO.

Economic dispatch (ED) is another critical issue in medium- and large-scale HPS management. In this regard, Xu and Yu [25] developed a solution using the multi-objective multi-verse optimizer algorithm (MOMVO), inspired by the multiverse theory's concepts of white holes, black holes, and wormholes. The authors validated MOMVO's effectiveness, noting good results in terms of convergence and overall performance compared to popular algorithms like NSGA-II.

Table 2 provides a summary of the MuOO algorithms discussed, including each methodology's strengths and limitations.

1.3. Research contributions

The range of HOTs for designing HPSs is extensive. Traditional methods with proven efficacy in minimizing TNPC, such as GA, PSO, DE, and SA, continue to be relevant in rural electrification projects. However, as previously discussed, modern techniques—such as the GOA, DO, COA, WOA, SCA, AVOA, GPC, BWO, QBWO, RLNNA, SDP, TLBO, LMAHA, AHA, GBO, ARO, and POA—offer high-quality solutions due to their advanced search capabilities.

For minimizing both TNPC and GHG emissions, NSGA-II and MOPSO, often used with TOPSIS, AHP, or fuzzy sets, remain widely accepted. The MuOO approaches have also been applied to enhance DS performance by minimizing PLs and improving voltage profiles. With recent technological advancements, newly developed methodologies—such as the ASSA, MOGWO, MORIME, MRFO, MOTEO, and MOMVO—have demonstrated excellent results.

As shown in Tables 1 and 2, considerable efforts have been made to incorporate renewable resource uncertainty through scenario generation and reduction and MCS or sensitivity analysis. Moreover, HOTs intrinsically cannot guarantee optimality, as they may stagnate around local optima. To address this issue, some researchers repeat the optimization process multiple times to reach alternative local optima. While this approach is essential for obtaining a robust solution, it is often limited due to its computational intensity. Additionally, most recent studies implement a BESS model of low complexity, which hinders accurate estimation of BESS replacement times, significantly affecting TNPC calculations.

Table 2
Key features of recent research on HPS management and design by MuOO.

Reference	Algorithm	Methodology
Sadeghibakhtiar et al. [1]	NSGA-II	The method accounts for uncertainties related to natural resources and equipment reliability. However, the reduction in BESS lifespan is not considered.
Cheraghi and Jahangir [13]	NSGA-II and MOPSO	It incorporates the HDI, which enhances optimization results and significantly reduces GHG emissions compared to fossil-fuel power plants. However, the implemented BESS model does not account for the complexities associated with replacement timing.
Ansari [14]	NSGA-II	It balances the cost and reliability of the HPS by accounting for natural resource uncertainty and system sensitivity.
Liu et al. [15]	NSGA-II	It incorporates a wide range of operating modes under uncertainty, including clean generation, energy storage, and DR resources. However, the computational model of the BESS is limited in estimating its lifespan.
Ahmed et al. [16]	ASSA	It enhances hydrothermal coordination by incorporating wind and solar resource uncertainties using RETScreen® software.
Belbachír et al. [17]	LMAHA, AHA, GBO, ARO, POA, PSO, GA, DE	The technique searches for the global optimum by independently repeating the optimization process 20 times. However, the optimization routine employs a simplified BESS model.
Mbasso et al. [18]	MOPSO, MOGWO, MOPSO-MOGWO	It utilizes two algorithms to achieve a high-quality solution. However, it employs a general-purpose BESS model that cannot estimate lifespan reduction due to charging and discharging cycles.
Hai et al. [19]	WOA-PS, TLBO, CSA	The method effectively minimizes operational uncertainty.
Alahmad et al. [20,21]	NSGA-II and MOPSO	It considers two storage technologies—BESS and CAES—along with DS restrictions and sources of uncertainty through PLF analysis. However, the BESS model is linearized to enhance the performance of the adopted optimization strategy, which limits accurate representation of the complex charging and discharging processes.
Pandya et al. [22,23]	MORIME, multi-objective WOA, GWO, and MRFO, among others	The techniques successfully resolved the OPF under uncertainty, considering DS restrictions such as VDs.
Agrawal et al. [24]	MOTEO, multi-objective WOA and GWO, among others	The approach provides a satisfactory solution to the OPF, accounting for the uncertainties of solar and wind resources, as well as DS operational constraints.
Xu and Yu [25]	MOMVO, NSGA-II, among others	It addresses ED by minimizing operating costs and GHG emissions, considering the valve-point effect of thermal generators and transmission system PLs.

Beyond the HOTs presented in Tables 1 and 2, various other techniques may be employed to solve the HPS design problem. In this paper, we introduce the Genghis Khan shark optimizer (GKSO) to HPS design for rural electrification. GKSO is a recently developed algorithm inspired by the predation and survival behaviors of Genghis Khan sharks. To the best of our knowledge, this is the first application of the GKSO algorithm to HPS dimensioning, representing a valuable contribution to existing literature.

To mitigate the increase in computational load due to uncertainty sources, we utilize a methodology commonly applied in neural network (NN) training. Using an autoregressive (AR) process, we generate scenarios of wind speed and solar radiation. Specifically, we create three sets of scenarios: training, validation, and testing. The training dataset, containing a limited number of scenarios, evaluates each agent's performance during the optimization process. The validation dataset, with a moderate number of scenarios, assesses the performance of the best-performing agent at each iteration, while the testing dataset evaluates the adopted configuration's performance. This approach allows us to reduce the computational effort required for evaluating all agents at each iteration, focusing resources on analyzing the best individual in each validation and, ultimately, testing phase. Additionally, for a lead-acid battery (LAB)-based storage system, we implement the weighted Ah throughput model complemented by some operational stress factors to enhance the reliability of TNPC estimation, an area typically under-explored in the literature according to Tables 1 and 2 Lastly, we perform an exhaustive search for the global optimum by repeating the optimization process multiple times, thereby approximating the probability of discovering new local optima through extended search optimization processes.

The paper is organized as follows: Section 2 describes the HPS simulation model, Section 3 explains the implementation of the proposed approach, Section 4 illustrates the approach with a rural electrification project, and Section 5 discusses the main findings and general conclusions.

2. Hybrid power system model

Typically, an HPS includes a wind turbine, a PV generator, a BESS based on lead-acid technology, a power converter, and a generator powered by gasoline or diesel. An energy system with these components is illustrated in Fig. 1. The conventional generator provides a controllable source to meet power demand. However, its continuous operation over time is neither economically nor environmentally advantageous. Integrating wind and solar PV energy reduces the operating hours of the conventional generator, leading to lower fuel consumption and decreased operating costs. The BESS stores excess renewable energy, which can be used later, further minimizing the reliance on the conventional thermal generator. The energy management system oversees the implementation of the operating strategy (load-following strategy) to manage the power available from renewable sources, the BESS, and the conventional generator.

The simulation and optimization model presented in this paper uses a set of scenarios, denoted by the index $s = 1, 2, \ldots, S$, to account for variability. This scenario set allows us to incorporate the variability of wind speed and solar irradiance over the years, along with the associated changes in each system component. Similarly, wind turbine manufacturers are represented by the index $z = 1, \ldots, Z$. PV panel manufacturers are represented by the index $v = 1,2,\ldots,V$. The index $m = 1, \ldots, M$ is used for each battery manufacturer, and $y = 1, \ldots, Y$ for each diesel or gasoline generator manufacturer.

The variable $P_{W(t,z,s)}$ represents the power output of the wind generator at time t, for manufacturer z and scenario s. Similarly, $P_{PV(t,v,s)}$ denotes the power output of the PV generator at time t, for manufacturer v and scenario s; $P_{BT(t,m,s)}$ represents the power output of the battery bank at time t, for manufacturer m and scenario s; and $P_{G(t,y,s)}$ represents the power output of the thermal generator at time t, for manufacturer y and scenario s. Finally, $P_{L(t)}$ denotes the power demand at time t. In the following sub-sections, we briefly describe the model for each element.

2.1. Wind turbine

The turbine manufacturer provides a numerical table that details the energy conversion process by relating wind speed to power production. Fig. 2 illustrates the typical shape of this curve, highlighting the cut-in, rated, and cut-out wind speeds. Power generation begins when the cut-in wind speed, typically between 3 m/s and 4 m/s, is reached. The rated power is produced at a corresponding wind speed, usually between 14 m/s and 15 m/s. Finally, at the cut-out speed, which ranges from 14 m/s to 18 m/s, power generation is limited to protect the turbine structure [26].

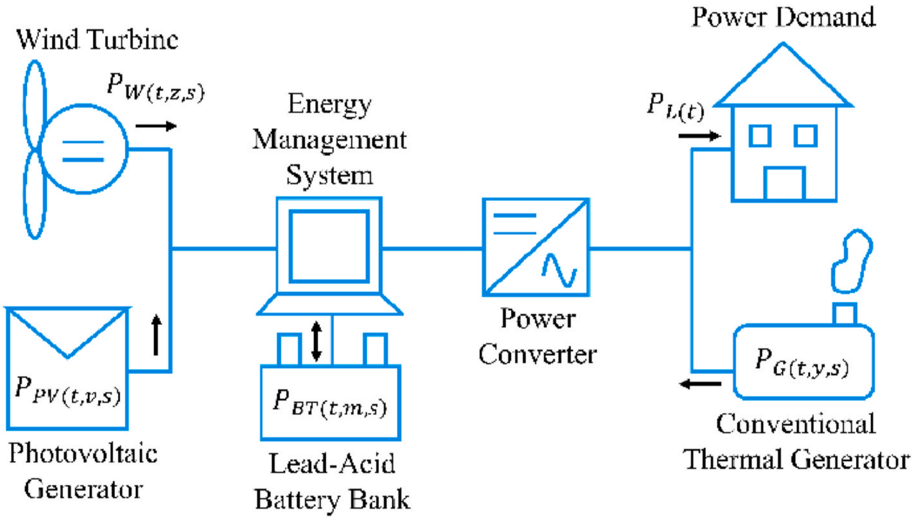

Fig. 1. Scheme of a hybrid power system.

To account for wind speed variability, several scenarios are considered. The variable $W_{(t,s)}$ represents the wind speed (m/s) at time t and scenario s. Assuming that the power curve in Fig. 2 corresponds to manufacturer z, the power production at time t ($p_{w(t,z,s)}$) can be estimated by applying $W_{(t,s)}$ to Fig. 2 through linear interpolation. The variable $p_{w(t,z,s)}$ represents the power production of a single turbine, while $P_{W(t,z,s)}$ in Fig. 1 represents the total power output of several turbines.

2.2. Photovoltaic generator

PV panel manufacturers often provide useful factors for estimating power production under various environmental conditions. Equations (1) and (2) can be used for this purpose [26]:

$$T_{C(t)} = T_{A(t)} + \left(\frac{NOCT_{(v)} - 20\,^{\circ}C}{800\ \mathrm{W/m^2}}\right) G_{(t,s)}, \tag{1}$$

$$p_{pv(t,v,s)} = P_{STC(v)} \left\{ \frac{G_{(t,s)}}{1000\ \mathrm{W/m^2}} \left[1 + \alpha_{PV(v)} \left(T_{C(t)} - 25\,^{\circ}C\right)\right] \right\}, \tag{2}$$

where, for a given manufacturer v, $NOCT_{(v)}$ is the nominal operating cell temperature (NOCT), $\alpha_{PV(v)}$ is the temperature coefficient of power for manufacturer v, $P_{STC(v)}$ is the power at standard test conditions (STC) for manufacturer v, and $T_{C(t)}$ is the cell temperature. The environmental conditions are represented by $G_{(t,s)}$, which is the solar irradiance at time t and scenario s, and $T_{A(t)}$, which is the ambient temperature. The variable $p_{pv(t,v,s)}$ represents the power generation of a single panel, while $P_{PV(t,v,s)}$ in Fig. 1 represents the power generation of several panels connected in parallel.

2.3. Lead-acid battery bank

The BESS is a crucial component that enhances system flexibility, enabling the consumption of clean energy when wind and solar resources are unavailable. LABs have been successfully used in rural electrification projects, so we focus particularly on this technology and the factors affecting its operating lifetime. On one hand, we used the weighted Ah throughput model [27–29] to quantitatively estimate LAB lifetime. On the other hand, we incorporated operating stress factors [27] to study LAB operation from a qualitative perspective. The details of these analyses are thoroughly discussed in the following sub-sections.

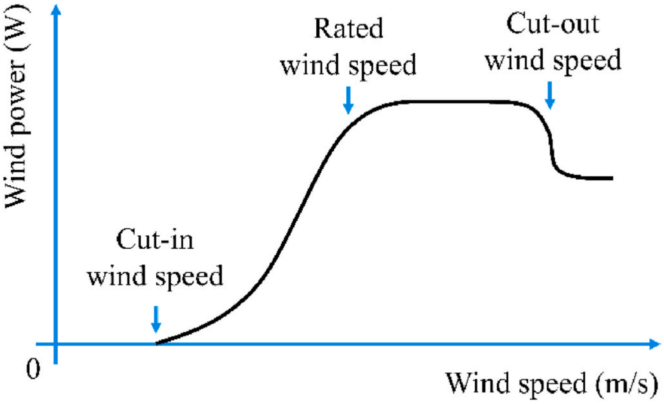

Fig. 2. Wind turbine power curve.

2.3.1. Modelling of a single cell

Shepherd's equation is commonly used to define the mathematical relationship between cell voltage $U_{(t,m,s)}$, current $I_{(t,m,s)}$, and state of charge (SOC) $SOC_{(t,m,s)}$ at any given time t, for manufacturer m and scenario s. Shepherd's equation accounts for open-circuit operation, resistive losses, and over-voltage. Equations (3) and (4) present the cell voltage for charging ($I_{(t,m,s)} > 0$) and discharging ($I_{(t,m,s)} \leq 0$) conditions [27–29]:

$$\begin{aligned} U_{(t,m,s)} = {} & U_{0(m)} - g_{(m)} DOD_{(t,m,s)} + R^{c}_{(t,m,s)} \left(\frac{I_{(t,m,s)}}{C_{10(m)}}\right) \\ & + R^{c}_{(t,m,s)} M_{c(m)} \left(\frac{I_{(t,m,s)}}{C_{10(m)}}\right) \left(\frac{SOC_{(t,m,s)}}{C_{c(m)} - SOC_{(t,m,s)}}\right) \ \forall\ I_{(t,m,s)} > 0, \end{aligned} \tag{3}$$

$$U_{(t,m,s)} = U_{0(m)} - g_{(m)} DOD_{(t,m,s)} + R^{d}_{(t,m,s)} \left(\frac{I_{(t,m,s)}}{C_{10(m)}}\right) + R^{d}_{(t,m,s)} M_{d(m)} \left(\frac{I_{(t,m,s)}}{C_{10(m)}}\right) \left(\frac{DOD_{(t,m,s)}}{C^{d}_{(t,m,s)} - DOD_{(t,m,s)}}\right) \ \forall\ I_{(t,m,s)} \leq 0.. \tag{4}$$

Some parameters vary with time, while others depend solely on the technology used by the manufacturer m. Specifically, $U_{0(m)}$ is the open-circuit voltage, $g_{(m)}$ is the open-circuit voltage variation with SOC, $R^{c}_{(t,m,s)}$ and $R^{d}_{(t,m,s)}$ are the charging and discharging resistances, respectively, and $M_{c(m)}$ and $M_{d(m)}$ are the resistances related to charge transfer during charging and discharging. $C_{c(m)}$ and $C^{d}_{(t,m,s)}$ are the normalized capacities. $DOD_{(t,m,s)}$ represents the depth of discharge (DOD), and $C_{10(m)}$ is the cell capacity over 10 h.

The gassing process, which is commonly observed during battery charging, is important for accurately estimating the SOC. It is incorporated into the SOC calculation in Equations (5) and (6) [27–29]:

$$SOC_{(t,m,s)} = SOC_{(t-\Delta t,m,s)} + \int_{t-\Delta t}^{t} \left\{ \frac{I_{(\tau,m,s)} - I^{G}_{(\tau,m,s)}}{C_{10(m)}} \right\} d\tau, \tag{5}$$

$$\begin{aligned} I^{G}_{(t,m,s)} = {} & \left(\frac{C_{10(m)}}{100} \right) \left(I^{G}_{0(t,m,s)} \right) exp \left(C_{U(m)} \left[U_{(t,m,s)} - U^{G}_{0(m)} \right] \right. \\ & \left. + C_{T(m)} \left[T_{A(t)} - T^{G}_{0(m)} \right] \right) \ \forall \ I_{(t,m,s)} > 0.. \end{aligned} \tag{6}$$

The gassing process is represented by the current $I^{G}_{(t,m,s)}$. Here, $C_{U(m)}$ is the voltage coefficient of gassing, $U^{G}_{0(m)}$ is the gassing voltage, $C_{T(m)}$ is the temperature coefficient of gassing, and $T^{G}_{0(m)}$ is the reference gassing temperature. All of these parameters correspond to the manufacturer m.

2.3.2. Modelling of positive grid corrosion

Shepherd's equation can also be used to describe the corrosion process. The corrosion during charging and discharging can be represented by Equations (7) and (8) [27–29]:

$$\begin{aligned} U^{c}_{(t,m,s)} = {} & U^{c}_{0(m)} - \left(\frac{10}{13} \right) g_{(m)} DOD_{(t,m,s)} + R^{c}_{(t,m,s)} \left(\frac{I_{(t,m,s)}}{2C_{10(m)}} \right) \\ & + R^{c}_{(t,m,s)} M_{c(m)} \left(\frac{I_{(t,m,s)}}{2C_{10(m)}} \right) \left(\frac{SOC_{(t,m,s)}}{C_{c(m)} - SOC_{(t,m,s)}} \right) \ \forall \ I_{(t,m,s)} > 0, \end{aligned} \tag{7}$$

$$U^{c}_{(t,m,s)} = U^{c}_{0(m)} - \left(\frac{10}{13} \right) g_{(m)} DOD_{(t,m,s)} + R^{d}_{(t,m,s)} \left(\frac{I_{(t,m,s)}}{2C_{10(m)}} \right) + R^{d}_{(t,m,s)} M_{d(m)} \left(\frac{I_{(t,m,s)}}{2C_{10(m)}} \right) \left(\frac{DOD_{(t,m,s)}}{C^{d}_{(t,m,s)} - DOD_{(t,m,s)}} \right) \ \forall \ I_{(t,m,s)} \leq 0, \tag{8}$$

where $U^{c}_{(t,m,s)}$ represents the corrosion voltage, and $U^{c}_{0(m)}$ is the corrosion voltage when the battery is fully charged. These variables vary according to the specific manufacturer and scenario of interest. The evolution of the corrosion layer is described by Equations (9)–(12) [27–29]:

$$\Delta\omega_{(t,m,s)} = \begin{cases} k_{sp} \left(\phi^{0.6} \right) \Big| \ \phi = \left[\Delta\omega_{(t-\Delta t,m,s)} / \left(k_{sp} \right) \right]^{\frac{1}{0.6}} + \Delta t; \ U^{c}_{(t,m,s)} \langle 1.74 < \\ \qquad \Delta\omega_{(t-\Delta t,m,s)} + \left(k_{sp} \right) \Delta t; \ U^{c}_{(t,m,s)} \geq 1.74 \end{cases}, \tag{9}$$

$$\Delta R_{(t,m,s)} = \Delta R_{max} \left(\frac{\Delta\omega_{(t,m,s)}}{\Delta\omega_{max(m)}} \right), \tag{10}$$

$$\Delta C^{c}_{(t,m,s)} = \Delta C^{c}_{max} \left(\frac{\Delta\omega_{(t,m,s)}}{\Delta\omega_{max(m)}} \right), \tag{11}$$

$$\Delta\omega_{max(m)} = 365 \times 24 \times \left(FL_{(m)} \right) \left(k^{sp}_{max(m)} \right), \tag{12}$$

where $\Delta\omega_{(t,m,s)}$ represents the corrosion layer thickness, k_{sp} is the speed coefficient of the corrosion process, $\Delta R_{(t,m,s)}$ denotes the internal resistance increment of the corrosion layer, ΔR_{max} is the maximum corrosion layer resistance, $\Delta\omega_{max\ (m)}$ represents the maximum corrosion layer thickness, $\Delta C^{c}_{(t,m,s)}$ is the loss of capacity due to the corrosion process, and ΔC^{c}_{max} is the maximum loss of capacity due to corrosion. The coefficient $k^{sp}_{max\ (m)}$ is the corrosion speed coefficient at the float voltage, determined through the Lander curve, and $FL_{(m)}$ represents the battery float life. These parameters are directly related to the time, manufacturer, and scenario under analysis.

2.3.3. Modelling of active mass degradation

The Ah throughput method utilizes key factors related to SOC, time spent at low SOC, discharging current, and incomplete charging cycles to estimate active mass degradation. These factors are defined in Equations (13)–(16), which are further illustrated in Fig. 3. In this figure, partial and full charging conditions are defined according to a threshold SOC value of 0.9 ($SOC^{max}_{lim} = 0.9$). The impact of time spent at low SOC is accounted for by the term $min\{SOC_{(\tau,m,s)} | \tau \in [t_{\beta(s)}, t]\}$ and $t - t_{\beta(s)}$. These concepts are incorporated into the SOC factor ($f^{soc}_{(t,m,s)}$) as shown in Equations (13) and (14) [27–29]:

$$f^{soc}_{(t,m,s)} = 1 + \left[c^{soc}_{0(m)} + c^{soc}_{min\ (m)} \left(1 - min\{SOC_{(\tau,m,s)} | \tau \in [t_{\beta(s)}, t]\} \right) f^{I}_{(t,m,s)} \Delta t^{soc}_{(t,s)} \right], \tag{13}$$

$$\Delta t^{soc}_{(t,s)} = t - t_{\beta(s)}, \tag{14}$$

where the coefficients $c^{soc}_{0(m)}$ and $c^{soc}_{min\ (m)}$ correspond to the slope and minimum SOC, respectively, while $\Delta t^{soc}_{(t,s)}$ represents the time since the last full charge.

The impact of the discharging current is accounted for by the current factor ($f^{I}_{(t,m,s)}$), which is defined in Equation (15) [27–29]:

$$f^{I}_{(t,m,s)} = \left(\sqrt{\frac{I_{r(m)}}{I^{1th}_{(t,m,s)}}} \right) \left(\sqrt[3]{exp \left(\frac{q_{(t,m,s)}}{3.6} \right)} \right), \tag{15}$$

where $I_{r(m)}$ is a reference value, and $I^{1th}_{(t,m,s)}$ represents the discharging current at the beginning of partial cycling. The variable $q_{(t,m,s)}$ denotes the number of cycles in which the full charging condition has not been met. The impact of insufficient charging is accounted for by weighting

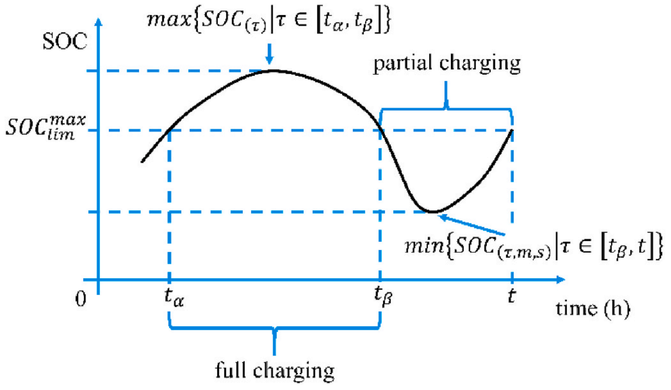

Fig. 3. Partial and full charging definitions.

the number of cycles according to the factor $\Delta q_{(t,m,s)}$, as defined in Equation (16), which incorporates the maximum SOC reached [27–29].

$$\Delta q_{(t,m,s)} = \frac{0.0025 - \left(0.95 - max\left\{SOC_{(\tau,m,s)} | \tau \in \left[t_\alpha, t_\beta\right]\right\}\right)^2}{0.0025}. \tag{16}$$

The gassing and diffusion processes are accounted for through the stratification factor ($f^{ST}_{(t,m,s)}$) defined in Equations (17)–(21). The term $min\left\{SOC_{(\tau,m,s)} | \tau \in \left[t_\beta, t\right]\right\}$ captures the effect of partial charging on the increase in acid stratification ($\Delta f^{+}_{(t,m,s)}$), while the gassing current ($I^{G}_{0(t,m,s)}$) is associated with the reduction in acid stratification ($\Delta f^{-}_{G(t,m,s)}$) as a result of the gassing and diffusion processes. The subtraction between these phenomena allows us to evaluate the influence of acid stratification on battery lifetime [27–29].

$$f^{ST}_{(t,m,s)} = f^{ST}_{(t-\Delta t,m,s)} + \int_{t-\Delta t}^{t} \left(\Delta f^{+}_{(\tau,m,s)} - \Delta f^{-}_{(\tau,m,s)}\right) d\tau, \tag{17}$$

$$\Delta f^{+}_{(t,m,s)} = C_{P(m)}\left(1 - min\left\{SOC_{(\tau,m,s)} | \tau \in \left[t_\beta, t\right]\right\}\right) exp\left(-3 f^{ST}_{(t,m,s)}\right)\left(\frac{\left|I^{d}_{(t,m,s)}\right|}{I_{r(m)}}\right), \tag{18}$$

$$\Delta f^{-}_{G(t,m,s)} = C_{M(m)} \sqrt{\frac{100}{C_{10(m)}}} \left(\frac{I^{G}_{0(t,m,s)}}{I^{G}_{0(m)}}\right) \exp\left(C_{U(m)}\left[U_{(t,m,s)} - U_{r(m)}\right] + C_{T(m)}\left[T_{A(t)} - T^{G}_{0(m)}\right]\right), \tag{19}$$

$$\Delta f^{-}_{D(t,m,s)} = \frac{8 D_{Z(m)}}{\left(Z_{D(m)}\right)^2} f^{ST}_{(t-\Delta t,m,s)} 2^{\left(T_{A(t)} - 293.15\right)/10}, \tag{20}$$

$$\Delta f^{-}_{(t,m,s)} = \Delta f^{-}_{D(t,m,s)} + \Delta f^{-}_{G(t,m,s)}. \tag{21}$$

In the acid stratification model, $I^{d}_{(t,m,s)}$ represents the discharging current, $C_{P(m)}$ is a parameter related to the acid stratification process, and $C_{M(m)}$ is a parameter associated with the reduction of acid stratification. $U_{r(m)}$ serves as a reference voltage for the acid stratification process, $D_{Z(m)}$ is a constant of the diffusion process, and $Z_{D(m)}$ represents the typical cell height. The term $\Delta f^{-}_{G(t,m,s)}$ relates to the reduction of acid stratification due to gassing, while $\Delta f^{-}_{D(t,m,s)}$ pertains to the reduction of acid stratification as a result of diffusion.

The cumulative effect of the increase and decrease in acid stratification is incorporated into the factor $f^{A}_{(t,m,s)}$, as defined by Equation (22) [27–29]:

$$f^{A}_{(t,m,s)} = 1 + f^{ST}_{(t,m,s)} \sqrt{\frac{I_{r(m)}}{I^{1th}_{(t,m,s)}}}. \tag{22}$$

The SOC factor ($f^{soc}_{(t,m,s)}$) and the acid stratification factor ($f^{A}_{(t,m,s)}$) are used to calculate the weighted *Ah* ($Z^{W}_{(t,m,s)}$) according to Equation (23) [27–29]:

$$Z^{W}_{(t,m,s)} = \frac{1}{C_{10(m)}} \int_{0}^{t} \left|I^{d}_{(t,m,s)}\right| f^{soc}_{(t,m,s)} f^{A}_{(t,m,s)} dt. \tag{23}$$

The capacity loss due to degradation ($\Delta C^{d}_{(t,m,s)}$) is calculated using Equation (24) [27–29]:

$$\Delta C^{d}_{(t,m,s)} = \Delta C^{d}_{max(m)}\, exp\left(-C_{Z(m)}\left\{1 - \frac{Z^{W}_{(t,m,s)}}{1.6\left[Z_{I(m)}\right]}\right\}\right), \tag{24}$$

where $\Delta C^{d}_{max(m)}$ is the maximum capacity loss related to battery degradation, $C_{Z(m)}$ is a coefficient related to the degradation process, and $Z_{I(m)}$ is the number of cycles under standard conditions for manufacturer *m*. Once the aging processes have been considered, the charging and discharging resistances ($R^{c}_{(t,m,s)}$ and $R^{d}_{(t,m,s)}$), the gassing current ($I^{G}_{0(t,m,s)}$), and the battery capacity ($C^{d}_{(t,m,s)}$) are updated using Equations (25)–(28) [27–29]:

$$R^{c}_{(t,m,s)} = R^{c}_{(0,m,s)} + \Delta R_{(t,m,s)} \tag{25}$$

$$R^{d}_{(t,m,s)} = R^{d}_{(0,m,s)} + \Delta R_{(t,m,s)} \tag{26}$$

$$I^{G}_{0(t,m,s)} = I^{G}_{0(m)} + \Delta I^{G}_{0(m)} \left(\frac{\Delta R_{(t,m,s)}}{\Delta R_{max\ (m)}}\right) \tag{27}$$

$$C^{d}_{(t,m,s)} = C^{d}_{(0,m,s)} - \Delta C^{c}_{(t,m,s)} - \Delta C^{d}_{(t,m,s)} \tag{28}$$

The simulation model described above is applied sequentially, estimating battery corrosion, active mass degradation, and parameter updates until the battery capacity drops below 0.8, at which point the battery is considered to have reached the end of its lifetime [27–29]. This time is stored in the variable *T*, and the stress factors are then assessed for $t = 1, 2, \ldots, T$.

2.3.4. *Operating stress factors*

LAB operation can be evaluated using stress factors such as the charge factor (CF), the *Ah* throughput, the highest discharge rate, the time between full charges and partial cycling, and the time spent at low SOC [30]. The following sub-sections briefly describe each of these factors.

2.3.4.1. Charge factor. The CF is useful for determining whether the battery is operating in full or partial mode. A very low CF could be associated with sulphation and acid stratification, while a very high CF indicates active mass shedding, water loss, and corrosion. The CF ($CF_{(m,s)}$) is calculated using Equations (29) and (30) [30]:

$$CF_{(m,s)} = \frac{Ah_{charged(m,s)}}{Ah_{discharged(m,s)}} = -\frac{\int_{t=1}^{T} I_{(\tau)} H\left(I_{(\tau,m,s)}\right) d\tau}{\int_{t=1}^{T} I_{(\tau)} H\left(-I_{(\tau,m,s)}\right) d\tau} \tag{29}$$

$$H\left(I_{(t,m,s)}\right) = \begin{cases} 0;\ I_{(t,m,s)} \langle 0 < \\ 1;\ I_{(t,m,s)} \geq 0 \end{cases} \forall\ t = 1, \ldots, T \tag{30}$$

where $Ah_{charged(m,s)}$ and $Ah_{discharged(m,s)}$ represent the ampere-hours charged and discharged, respectively, and $H(\cdot)$ is the Heaviside function.

2.3.4.2. Ah throughput. The Ah throughput estimates the ampere-hours discharged over the period of interest. This factor complements other parameters related to partial cycling operation and its duration. The *Ah* throughput ($Q_{thr(m,s)}$) is defined in Equation (31) [30]:

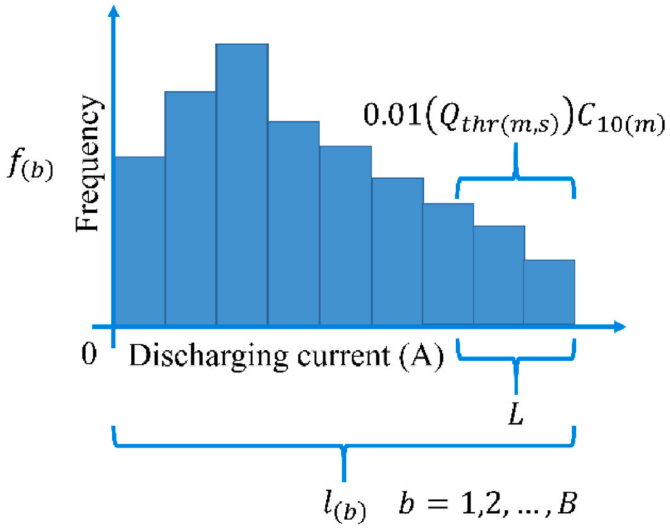

Fig. 4. Histogram of discharge current.

$$Q_{thr(m,s)} = \frac{\int_{t=1}^{T} I_{(t,m,s)} H(-I_{(t,m,s)})}{C_{10(m)}} \tag{31}$$

2.3.4.3. Highest discharge rate. To assess the impact of the highest discharge rate, a discharged-current histogram is constructed using B bins, as shown in Fig. 4. Next, we identify the bins (L) that account for 1 % of the total Ah throughput discharged over the period under study. Finally, the highest discharge rate ($I^{max}_{1\%(m,s)}$) is calculated using Equations (32) and (33) [30]:

$$\sum_{b=B-L}^{B} l_{(b)} f_{(b)} = 0.01\left(Q_{thr(m,s)}\right)C_{10(m)} \tag{32}$$

$$I^{max}_{1\%(m,s)} = \left\{0.01\left(Q_{thr(m,s)}\right)C_{10(m)}\right\} \Big/ \left\{I_{10(m)}\left(\sum_{b=B-L}^{B} l_{(b)} f_{(b)}\right)\right\} \tag{33}$$

where $I_{10(m)}$ is the discharging current in 10 h.

2.3.4.4. Time between full charge. The time between full charges ($T_{F(m,s)}$) is directly determined by the periods when the SOC is lower than the threshold $SOC^{max}_{lim} = 0.9$ and the duration of these periods. Therefore, calculating the number of cycles ($C_{F(m,s)}$) is crucial. This factor is defined by Equation (34) [30]:

$$T_{F(m,s)} = \left\{\int_{t=1}^{T} H\left(SOC^{max}_{lim} - SOC_{(\tau,m,s)}\right)d\tau\right\} \Big/ \left\{24\left(C_{F(m,s)}\right)\right\} \tag{34}$$

2.3.4.5. Partial cycling. Partial cycling (PC) enables us to account for the effects of discharging the battery at different SOC levels. Therefore, we first need to determine the SOC levels (A, B, C, D, and E) using Table 3, represented by the variable x. Then, PC ($PC_{(m,s)}$) is calculated using Equations (35) and (36) [30]:

$$P_{(x,m,s)} = \frac{-\left\{\int_{t=1}^{T} I_{(\tau)} H\left(P^{min}_{(x)} - SOC_{(\tau,m,s)}\right) H\left(P^{max}_{(x)} - SOC_{(\tau,m,s)}\right) H\left(-I_{(\tau,m,s)}\right)d\tau\right\}}{\left\{\int_{t=1}^{T} I_{(\tau,m,s)} H\left(-I_{(\tau,m,s)}\right)d\tau\right\}} \quad \forall\, x = A, B, C, D, E \tag{35}$$

Table 3
State-of-charge intervals.

x	$P^{min}_{(x)}$	$P^{max}_{(x)}$
A	0.85	1
B	0.7	0.85
C	0.55	0.7
D	0.4	0.55
E	0	0.4

$$PC_{(m,s)} = \left\{P_{(A,m,s)} + 2\left[P_{(B,m,s)}\right] + 3\left[P_{(C,m,s)}\right] + 4\left[P_{(D,m,s)}\right] + 5\left[P_{(E,m,s)}\right]\right\} / 5 \tag{36}$$

2.3.4.6. Time at low SOC. The time at low SOC ($T_{S(m,s)}$) is a stress factor used to analyze situations when the SOC falls below a specific threshold, $SOC^{min}_{lim} = 0.35$. This factor is calculated using Equation (37) [30]:

$$T_{S(m,s)} = \frac{100}{T}\left\{\int_{t=1}^{T} H\left(SOC^{low}_{lim} - SOC_{(\tau,m,s)}\right)d\tau\right\}. \tag{37}$$

Fig. 5 summarizes the process of battery lifetime estimation and stress factor calculation. First, we use the weighted *Ah* throughput model to estimate the battery lifetime (T) in hours, taking into account corrosion and active mass degradation. Next, we evaluate the operating stress factors to gain a general understanding of the mechanisms involved in lifetime reduction. These approaches provide both a quantitative perspective, necessary for TNPC estimation, and a qualitative understanding of the phenomena contributing to lifetime loss.

2.4. *Power converter*

The power converter connects devices operating on direct current (DC) to those functioning on alternating current (AC). The model used here focuses on the power converter efficiency ($\eta_{conv(t,s)}$), which varies according to Equation (38):

$$\eta_{conv(t,s)} = \frac{P_{conv(t,s)}}{\xi_{conv} \times P^{max}_{conv} + \lambda_{conv} \times P_{conv(t,s)}}, \tag{38}$$

where ξ_{conv} and λ_{conv} are model parameters, P^{max}_{conv} is the converter's rated power, and $P_{conv(t,s)}$ is the power flowing through the converter. Equation (38) simplifies a more complex model, allowing us to avoid solving nonlinear equations and thus reducing computational effort. A comprehensive analysis of power converter efficiency models is provided in Ref. [31].

2.5. *Conventional thermal generator*

A conventional generator significantly improves system reliability. The model used in this work focuses on calculating fuel consumption, which is done using Equation (39):

$$F_{g(t,y,s)} = \gamma_{g(y)} \times P^{max}_{g(y)} + \chi_{g(y)} \times P_{g(t,y,s)}, \tag{39}$$

where $F_{g(t,y,s)}$ represents the fuel consumption (diesel or gasoline) for manufacturer y, at time t and scenario s. $\gamma_{g(y)}$ and $\chi_{g(y)}$ are parameters derived from experimental measurements.

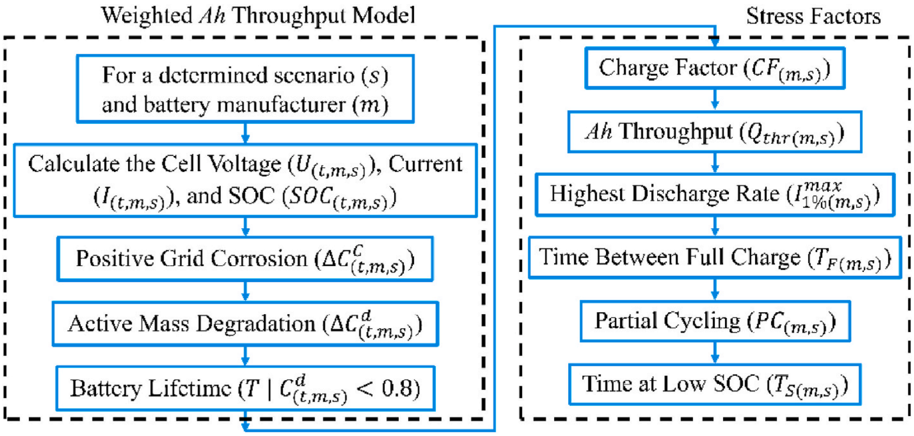

Fig. 5. Estimation of the battery lifetime and the operating stress factors.

3. Proposed optimization model

The design technique proposed in this paper involves determining the optimal size of the wind and PV generators, BESS, power converter, and conventional generator to minimize TNPC. The optimization problem is addressed by considering the variability of wind speed and solar irradiance to achieve a reliable design. Details of the optimization process are explained in the following sub-sections.

3.1. Mathematical basis of the design problem

The optimal design problem involves minimizing TNPC, which is estimated over the project's lifetime. TNPC includes the capital and replacement costs of the equipment, as well as operating and maintenance (O&M) costs. The lifetimes of some devices, such as the BESS and conventional generators, depend on renewable resources. The variability of wind speed and solar irradiance affects the battery discharging current, which in turn influences its lifetime. Similarly, the running hours of diesel or gasoline generators are affected by net-load variability, impacting the operating life of the generation unit. In general, the variability of environmental resources directly impacts TNPC estimation. Equation (40) expresses the goal of minimizing TNPC. The variable $\boldsymbol{a}$ is a vector representing a specific combination of wind turbines, PV panels, BESS, and the conventional generator. Resource variability is accounted for through scenarios, allowing us to estimate the average TNPC ($TNPC^{avg}_{(\boldsymbol{a})}$) for a given system architecture ($\boldsymbol{a}$) as shown in Equation (41). $TNPC_{(\boldsymbol{a},s)}$ represents the TNPC obtained from each scenario ($s = 1,\ldots,S$) separately.

$$min\{TNPC^{avg}_{(\boldsymbol{a})}\}, \tag{40}$$

$$TNPC^{avg}_{(\boldsymbol{a})} = \frac{1}{S}\sum_{s=1}^{S} TNPC_{(\boldsymbol{a},s)}. \tag{41}$$

System reliability is measured using the energy index of unreliability (EIU), which is the ratio between energy losses and the total energy to be supplied. Reliability is incorporated into the optimization problem through the constraint in Equation (42), where EIU_{avg} is the average EIU calculated using Equation (43), and EIU_{trg} is the target or required EIU set by the system designer. $EIU_{(\boldsymbol{a},s)}$ represents the EIU obtained from each scenario ($s = 1,\ldots,S$) separately.

$$EIU_{avg} \le EIU_{trg}, \tag{42}$$

$$EIU_{avg} = \frac{1}{S}\sum_{s=1}^{S} EIU_{(\boldsymbol{a},s)}. \tag{43}$$

The operating constraints of each device must be met under all conditions. For the BESS, restrictions on the battery SOC, cell current, and voltage are presented in Equations (44)–(46). Here, $SOC_{min\ (m)}$ represents the minimum SOC, $I^{min}_{bt(m)}$ are the minimum and maximum cell currents, and $U^{min}_{bt(m)}$ and $U^{max}_{bt(m)}$ are the minimum and maximum cell voltages. These variables are derived from the weighted Ah throughput model previously explained.

$$SOC_{min\ (m)} \le SOC_{(t,m,s)} \le 1, \tag{44}$$

$$I^{min}_{bt(m)} \le I_{(t,m,s)} \le I^{max}_{bt(m)}, \tag{45}$$

$$U^{min}_{bt(m)} \le U_{(t,m,s)} \le U^{max}_{bt(m)}. \tag{46}$$

The operating stress factors are incorporated into the design process through the constraints in Equations (47)–(52). Here, $CF^{avg}_{(m)}$, Q^{avg}_{thr}, $I^{max,avg}_{1\%(m)}$, $T^{avg}_{F(m)}$, $PC^{avg}_{(m)}$, and $T^{avg}_{S(m)}$ represent the average values for CF, Ah throughput, highest discharge rate, time between full charges, partial cycling, and time at low SOC, respectively. Similarly, CF_{trg}, Q^{trg}_{thr}, $I^{max,trg}_{1\%}$, T^{trg}_{F}, PC_{trg}, and T^{trg}_{S} are the target values for each stress factor. The numerical values considered are shown in Table 4 and correspond to those of an optimal solar home system (SHS). In other words, we aim to achieve operational performance similar to that of an optimal SHS from a qualitative perspective [30].

$$CF^{avg}_{(m)} = \frac{1}{S}\sum_{s=1}^{S} CF_{(m,s)} \le CF_{trg}, \tag{47}$$

$$Q^{avg}_{thr} = \frac{1}{S}\sum_{s=1}^{S} Q_{thr(m,s)} \le Q^{trg}_{thr}, \tag{48}$$

$$I^{max,avg}_{1\%(m)} = \frac{1}{S}\sum_{s=1}^{S} I^{max}_{1\%(m,s)} \le I^{max,trg}_{1\%}, \tag{49}$$

$$T^{avg}_{F(m)} = \frac{1}{S}\sum_{s=1}^{S} T_{F(m,s)} \le T^{trg}_{F}, \tag{50}$$

$$PC^{avg}_{(m)} = \frac{1}{S}\sum_{s=1}^{S} PC_{(m,s)} \le PC_{trg}, \tag{51}$$

Table 4
Target values for stress factors.

CF_{trg}	Q^{trg}_{thr}	$I^{max,trg}_{1\%}$	T^{trg}_{F}	PC_{trg}	T^{trg}_{S}
115 %	70	1.4	8 days	70 %	15.5 %

$$T^{avg}_{S(m)} = \frac{1}{S}\sum_{s=1}^{S} T_{S(m,s)} \le T^{trg}_{S}. \tag{52}$$

The constraint in Equation (53) is incorporated to ensure the safe operation of the power converter. It is important to note that there is no specific power converter manufacturer considered, as its capacity (P^{max}_{conv}) has been set to match the maximum power demand.

$$0 \le P_{conv(t,s)} \le P^{max}_{conv}. \tag{53}$$

Conventional generators typically need to operate within a specific power output range. Equation (54) defines this restriction, where $P^{min}_{g(y)}$ and $P^{max}_{g(y)}$ represent the minimum and maximum output power specified by manufacturer y.

$$P^{min}_{g(y)} \le P_{g(t,y,s)} \le P^{max}_{g(y)}. \tag{54}$$

Equations (55)–(58) represent the system power balance, where j is the number of wind turbines, d is the number of PV strings in parallel, o is the number of LAB strings in parallel, and $p_{bt(t,m,s)}$ is the power of a LAB string.

$$j \times p_{w(t,z,s)} + d \times p_{pv(t,v,s)} \pm o \times p_{bt(t,m,s)} + ENS_{(t,s)} - \left(P_{L(t)} + ES_{(t,s)}\right) = P_{g(t,y,s)}, \tag{55}$$

$$P_{W(t,z,s)} + P_{PV(t,v,s)} \pm P_{BT(t,m,s)} + ENS_{(t,s)} - \left(P_{L(t)} + ES_{(t,s)}\right) = P_{g(t,y,s)}, \tag{56}$$

$$0 \le ENS_{(t,s)} \le \infty, \tag{57}$$

$$0 \le ES_{(t,s)} \le \infty. \tag{58}$$

In other words, the power output of the wind generator ($P_{W(t,z,s)}$), the PV generator ($P_{PV(t,v,s)}$), and the BESS ($P_{BT(t,m,s)}$) are expressed as $P_{W(t,z,s)} = j \times p_{w(t,z,s)}$, $P_{PV(t,v,s)} = d \times p_{pv(t,v,s)}$, and $P_{BT(t,m,s)} = o \times p_{bt(t,m,s)}$, resulting in the expression in Equation (56). Additionally, the variables $ENS_{(t,s)}$ and $ES_{(t,s)}$ represent the energy not supplied (ENS) and energy surplus, respectively. ENS is directly related to the EIU and is crucial for evaluating the constraint in Equation (42). As shown in Equations (57) and (58), $ENS_{(t,s)}$ and $ES_{(t,s)}$ are constrained to be positive.

3.2. Modelling the variability of environmental resources

As mentioned above, the variability of wind speed and solar irradiance is incorporated into the optimization problem through scenarios. These scenarios are simulated while maintaining the most important statistical characteristics of the available time series. This task can be performed using Markov-chain theory, wavelet or Fourier decomposition, and an AR process. In this work, we apply a first-order AR process to simulate wind speed and solar irradiance time series. The simulation process is described for wind speed, but it can also be applied to solar irradiance using a similar procedure. The time series simulation process is implemented as follows [32].

Step 1 Apply a probability transformation from the original distribution to a Gaussian distribution with a mean of zero and a standard deviation of one. Assuming $W^{tmy}_{(t)}$ represents the typical meteorological year (TMY) of wind speed, the transformation is applied according to Equation (59). The function CDF_{tmy} is the cumulative distribution function (CDF) of $W^{tmy}_{(t)}$, CDF^{-1}_{Gauss} is the inverse CDF of a Gaussian distribution with a mean of zero and a standard deviation of one, and $W^{trs}_{(t)}$ represents the transformed wind speed time series.

$$W^{trs}_{(t)} = CDF^{-1}_{Gauss}\left(CDF_{tmy}\left(W^{tmy}_{(t)}\right)\right), \tag{59}$$

Step 2 Remove the diurnal non-stationarity of the transformed series ($W^{trs}_{(t)}$) by subtracting its hourly mean ($\mu_{trs(h)}$) and standard deviation ($\sigma_{trs(h)}$) for $h = 1, \ldots, 24$ as shown in Equation (60). The result, $W^{Gauss}_{(t)}$, is the transformed and normalized time series.

$$W^{Gauss}_{(t)} = \frac{W^{trs}_{(t)} - \mu_{trs(h)}}{\sigma_{trs(h)}}. \tag{60}$$

Step 3 Determine the one-lag autocorrelation coefficient (ρ_{AR}) of the series $W^{Gauss}_{(t)}$ obtained in Step 2. Then, generate S time series using Equation (61). The variable $x^{Gauss}_{(t,s)}$ follows a Gaussian distribution with autocorrelation ρ_{AR}, while $RANG$ is a random number drawn from a Gaussian distribution with a mean of zero and a standard deviation of $\sqrt{1-(\rho_{AR})^2}$.

$$x^{Gauss}_{(t,s)} = x^{Gauss}_{(t-1,s)} + RANG\left(0, \sqrt{1-(\rho_{AR})^2}\right), \tag{61}$$

Step 4 The procedure applied so far is performed in reverse on $x^{Gauss}_{(t,s)}$. To do this, we apply Equation (62). The function CDF_{scn} is the CDF of the time series $x^{Gauss}_{(t,s)}\sigma_{trs(h)} + \mu_{trs(h)}$, and CDF^{-1}_{wfit} is the inverse CDF of a Weibull distribution (for wind speed) or a Beta distribution (for solar irradiance), both obtained from TMY. Finally, $W_{(t,s)}$ represents the simulated wind speed time series for scenario $s = 1, \ldots, S$.

$$W_{(t,s)} = CDF^{-1}_{wfit}\left(CDF_{scn}\left(x^{Gauss}_{(t,s)}\sigma_{trs(h)} + \mu_{trs(h)}\right)\right) \tag{62}$$

This methodology is used to create the training, validation, and testing sets of wind speed and solar irradiance scenarios for the optimization process. The number of scenarios in the testing set should be larger than those in the validation and training sets, although this depends heavily on the available computational resources.

3.3. Integer-coded Genghis Khan Shark Optimizer

The agents play a crucial role in the optimization process. In this paper, each agent is structured as a vector, as shown in Equation (63) and detailed in Table 5. The elements of the vector are carefully explained. When the corresponding index (v, d, z, j, m, o, and y) is set to 1, it assigns a value of zero to the corresponding device. For example, if v is set to 1 ($v = 1$), it indicates that no PV panel is considered.

$$\boldsymbol{a}_{(i)} = \left[\begin{matrix} v & d & z & j & m & o & y \end{matrix}\right] \tag{63}$$

The population ($\boldsymbol{x}^{gkso}_{int}$) is then constructed by assembling I agents in a tabular form, as shown in Equation (64).

$$\boldsymbol{x}^{gkso}_{int} = \begin{bmatrix} \vdots \\ \boldsymbol{a}_{(i)} \\ \vdots \end{bmatrix} \tag{64}$$

The Genghis Khan Shark Optimizer (GKSO) [33] is a recently developed algorithm designed to solve complex optimization problems.

Table 5
Description of a GKSO agent.

Element of agent $\boldsymbol{a}_{(i)}$	Description
$v \in [2, V+1]$	Index for solar panel manufacturers
$d \in [2, D+1]$	Number of panels in parallel
$z \in [2, Z+1]$	Index for wind turbine manufacturers
$j \in [2, J+1]$	Number of wind turbines
$m \in [2, M+1]$	Index for battery manufacturers
$o \in [2, O+1]$	Number of batteries in parallel
$y \in [2, Y+1]$	Index for generator manufacturers

It is inspired by the behavior of Genghis Khan sharks, particularly their actions during the hunting, moving, foraging, and escaping phases. GKSO is computationally implemented in four steps: wandering hunting stage, moving towards the best hunting position, parabolic foraging, and self-protection mechanism. It is important to note that, according to Equation (63), the population is encoded using integer numbers. All GKSO-related operations are then applied using binary coding. In other words, the implementation used in this work is intrinsically binary, necessitating a conversion process between integer and binary numbers, and vice versa.

3.3.1. *Wandering hunting stage*

It is inspired by the patrolling behavior of Genghis Khan sharks, which ensures there are no other predators in their territory. From a computational perspective, this behavior is understood as the exploration phase. The wandering hunting stage, or exploration phase, is implemented as follows [33].

Step 1 Set the number of agents (I) and iterations (K) for the optimization process.

Step 2 Initialize the algorithm using a random number generator to obtain the population $\boldsymbol{x}^{gkso}_{int}$. Each row ($\boldsymbol{a}_{(i)}\ \forall\, i = 1, \dots, I$) represents an agent in the optimization process.

Step 3 Evaluate the population by obtaining the corresponding objective function value (TNPC) for each agent. To do this, simulate the HPS to calculate the average TNPC ($TNPC^{avg}_{(\boldsymbol{a})}$) for each agent ($\boldsymbol{a}_{(i)}\ \forall\, i = 1, \dots, I$) in the population.

Step 4 Convert the agents of the population obtained in Step 2 ($\boldsymbol{a}_{(i)}\ \forall\, i = 1, \dots, I$) into binary form. This will result in a binary-coded population ($\boldsymbol{x}^{gkso}_{bin}$) with I rows and N columns. N is determined by the number of bits required to represent the corresponding integers (Table 5) as binary strings.

Step 5 Apply the operator in Equation (65), where $lb_{(n)}$ and $ub_{(n)}$ are the lower and $x^{gkso}_{bin(i,n)}$, which are zero and one, respectively. k is the current iteration, and $RAND$ is a uniform random number in the interval [0,1].

$$x^{gkso}_{bin(i,n)} = x^{gkso}_{bin(i,n)} + \frac{lb_{(n)} + RAND \times \left(ub_{(n)} - lb_{(n)}\right)}{k}. \tag{65}$$

Step 6 Convert the variables $x^{gkso}_{bin(i,n)}$ from Step 5 to either zero or one by selecting the closest value between these two options, resulting in a binary population.

Step 7 Convert the binary population $\boldsymbol{x}^{gkso}_{bin}$ into an integer population, resulting in $\boldsymbol{x}^{gkso}_{int}$, which has a structure similar to that of Equation (64).

Step 8 Limit the elements of the population $\boldsymbol{x}^{gkso}_{int}$ obtained in Step 7 to their corresponding boundaries as specified in Table 3.

Step 9 Evaluate the population from Step 8 using the training scenario set to obtain the corresponding objective function value (TNPC) for each agent. To do this, simulate the HPS considering the training scenario set, and calculate the average TNPC ($TNPC^{avg}_{(\boldsymbol{a})}$) for each agent ($\boldsymbol{a}_{(i)}\ \forall\, i = 1, \dots, I$) in the population.

Step 10 Compare the population obtained in Step 3 with that obtained in Step 8 based on fitness (TNPC) and select the best agents. Sequentially compare each agent ($i = 1, \dots, I$) from the population of Step 3 with the corresponding agent from the population of Step 8, and select the option with the lowest TNPC. This results in the population obtained from the wandering hunting stage.

3.3.2. *Moving towards the best hunting position*

It is inspired by the sensitivity of Genghis Khan sharks to recognize and approach the best prey. From an optimization perspective, this is understood as the exploitation phase. This stage is implemented by following these steps.

Step 1 Convert the population obtained in the final step of the wandering hunting stage (Step 10) into a binary-coded population $x^{gkso}_{bin(i,n)}\ \forall\, i = 1, \dots, I; n = 1, \dots, N$.

Step 2 Calculate the attractiveness model ($s^{gkso}_{(i)}\ \forall\, i = 1, \dots, I$) according to Equation (66), where $RAND$ is a uniform random number in the interval [0,1], and $TNPC^{avg}_{(\boldsymbol{a})}$ is the TNPC of individual i.

$$s^{gkso}_{(i)} = 1.5\left(TNPC^{avg}_{(\boldsymbol{a})}\right)^{RAND}\ \forall\, i = 1, \dots, I. \tag{66}$$

Step 3 Apply the operator described in Equation (67), where the operation $.\times$ is similar to the conventional dot-product.

$$\boldsymbol{x}^{gkso}_{bin(i,:)} \leftarrow \begin{cases} s^{gkso}_{(i)} .\times \left(\boldsymbol{x}^{gkso}_{best} - \boldsymbol{x}^{gkso}_{bin(i,:)}\right); i = 1 \\ \begin{cases} \boldsymbol{x}_{aux} = s^{gkso}_{(i)} .\times \left(\boldsymbol{x}^{gkso}_{best} - \boldsymbol{x}^{gkso}_{bin(i,:)}\right) \\ \left(\boldsymbol{x}_{aux} + \boldsymbol{x}^{gkso}_{bin(i-1,:)}\right) .\times \dfrac{1}{2} \end{cases} ; i \neq 1 \end{cases} \tag{67}$$

Step 4 Convert the population $\boldsymbol{x}^{gkso}_{bin}$ from Step 3 to either zero or one by selecting the closest value between these two options, resulting in a binary population.

Step 5 Convert the binary population $\boldsymbol{x}^{gkso}_{bin}$ into an integer population, resulting in $\boldsymbol{x}^{gkso}_{int}$, with a structure similar to that in Equation (64).

Step 6 Limit the elements of the population $\boldsymbol{x}^{gkso}_{int}$ obtained in Step 5 to their corresponding bounds, as specified in Table 3.

Step 7 Evaluate the population from Step 6 using the training scenario set to obtain the corresponding objective function value (TNPC) for each agent. To do this, simulate the HPS considering the training scenario set and calculate the average TNPC ($TNPC^{avg}_{(\boldsymbol{a})}$) in the population.

Step 8 Compare the population obtained in Step 1 with that obtained in Step 6 based on fitness (TNPC) and select the best agents. Sequentially compare each agent ($i = 1, \dots, I$) from the population of Step 1 with the corresponding agent from the population of Step 6 and select the option with the lowest TNPC. This results in the population obtained from the 'moving towards the best hunting position' stage.

3.3.3. *Parabolic foraging*

It is inspired by the way Genghis Khan sharks organize once they have identified their prey. This organizational process follows a parabolic pattern. Parabolic foraging is computationally implemented as follows.

Step 1 Convert the population obtained in the final step of the 'moving towards the best hunting position' stage (Step 8) into a binary-coded population $x^{gkso}_{bin(i,n)}\ \forall\, i = 1, \dots, I; n = 1, \dots, N$.

Step 2 Calculate the parameters ε_{gkso} and p_{gkso} according to Equations (68) and (69):

$$\varepsilon_{gkso} \leftarrow \begin{cases} 0.1; k = 1 \\ 1 - 2\left(\varepsilon_{gkso}\right)^4; k \neq 1 \end{cases}, \tag{68}$$

$$p_{gkso} = 2\left\{1 - \left(\frac{k}{K}\right)^{1/4}\right\} + \left|\varepsilon_{gkso}\right|\left\{\left(\frac{k}{K}\right)^{1/4} - \left(\frac{k}{K}\right)^3\right\}. \tag{69}$$

Step 3 Apply the operator described in Equation (70), where the operation $.\times$ is similar to the conventional dot-product.

$$\boldsymbol{x}^{gkso}_{bin(i,:)} \leftarrow \boldsymbol{x}^{gkso}_{best} + \boldsymbol{RAND}.\times\left(\boldsymbol{x}^{gkso}_{best} - \boldsymbol{x}^{gkso}_{bin(i,:)}\right) + \lambda_{gkso}\left(p_{gkso}\right)^2. \times\left(\boldsymbol{x}^{gkso}_{best} - \boldsymbol{x}^{gkso}_{bin(i,:)}\right) \tag{70}$$

Step 4 Convert the population $\boldsymbol{x}^{gkso}_{bin}$ from Step 3 to either zero or one by selecting the closest value between these two options, resulting in a binary population.

Step 5 Convert the binary population $\boldsymbol{x}^{gkso}_{bin}$ into an integer population, resulting in $\boldsymbol{x}^{gkso}_{int}$, with a structure similar to that in Equation (64).

Step 6 Limit the elements of the population $\boldsymbol{x}^{gkso}_{int}$ obtained in Step 5 to their corresponding bounds, as specified in Table 3.

Step 7 Evaluate the population from Step 6 using the training scenario set to obtain the corresponding objective function value (TNPC) for each agent. To do this, simulate the HPS considering the training scenario set and calculate the average TNPC ($TNPC^{avg}_{(\boldsymbol{a})}$) for each agent ($\boldsymbol{a}_{(i)}\ \forall\ i = 1,\ldots,I$) in the population.

Step 8 Compare the population obtained in Step 1 with that obtained in Step 6 based on fitness (TNPC) and select the best agents. Sequentially compare each agent ($i = 1,\ldots,I$) from the population in Step 1 with the corresponding agent from the population in Step 6, and select the option with the lowest TNPC. This results in the population obtained from the parabolic foraging stage.

3.3.4. Self-protection mechanism

It is inspired by the Genghis Khan sharks' ability to avoid enemies through their color-changing mechanism. The self-protection mechanism is implemented by following these steps.

Step 1 Convert the population obtained in the final step of the parabolic foraging stage (Step 8) into a binary-coded population $x^{gkso}_{bin(i,n)}\ \forall\ i = 1,\ldots,I; n = 1,\ldots,N.$

Step 2 Calculate the parameters β_{gkso}, α_{gkso}, and ρ_{gkso} using Equations (71)–(73):

$$\beta_{gkso} = \beta^{min}_{gkso} + \left(\beta^{max}_{gkso} - \beta^{min}_{gkso}\right)\left(1 - \left(\frac{k}{K}\right)^3\right)^2, \tag{71}$$

$$\alpha_{gkso} = \left|\beta_{gkso}\ sin\left(\frac{3\pi}{2} + sin\left(\frac{3\pi}{2}\beta_{gkso}\right)\right)\right|, \tag{72}$$

$$\rho_{gkso} = \alpha_{gkso}(2 \times RAND - 1). \tag{73}$$

Step 3 For each agent in the population ($i = 1, \ldots, I$), calculate the vectors $\boldsymbol{X1}, \boldsymbol{X2}, \boldsymbol{Xr}, \boldsymbol{Xp}, \boldsymbol{Xk}, \boldsymbol{Xu1}, \boldsymbol{Xu2}$ using Equations (74)–(81). Then, update the population $\boldsymbol{x}^{gkso}_{bin(i,:)}$ based on a random event. If a_1 is less than 0.5, update the agent $\boldsymbol{x}^{gkso}_{bin(i,:)}$ using Equation (82); otherwise, use Equation (83). Here, a_1 is a uniform random number in the interval [0,1], and $RANI$ is an integer random number in the interval $[1, I]$. The variables a_2, a_3, $l1$, and $l2$ are random numbers.

$$X1_{(n)} = lb_{(n)} + RAND \times (ub_{(n)} - lb_{(n)})\ \forall\ n = 1,\ldots,N \tag{74}$$

$$X2_{(n)} = lb_{(n)} + RAND \times (ub_{(n)} - lb_{(n)})\ \forall\ n = 1,\ldots,N \tag{75}$$

$$\boldsymbol{Xr} = \boldsymbol{x}^{gkso}_{bin(RANI,:)} \tag{76}$$

$$Xp_{(n)} = lb_{(n)} + RAND \times (ub_{(n)} - lb_{(n)})\ \forall\ n = 1,\ldots,N \tag{77}$$

$$\begin{cases} a_1 = l1 \times 2 \times RAND + (1 - l1) \\ a_2 = l1 \times RAND + (1 - l1) \\ a_3 = l1 \times RAND + (1 - l1) \end{cases} \tag{78}$$

$$\boldsymbol{Xk} = l2. \times \boldsymbol{Xp} + (1 - l2). \times \boldsymbol{Xr} \tag{79}$$

$$\boldsymbol{Xu1} = \boldsymbol{x}^{gkso}_{bin(RANI,:)} \tag{80}$$

$$\boldsymbol{Xu2} = \boldsymbol{x}^{gkso}_{bin(RANI,:)} \tag{81}$$

$$\boldsymbol{x}^{gkso}_{bin(i,:)} \leftarrow \boldsymbol{x}^{gkso}_{bin(i,:)} + k_1. \times \left(a_1. \times \boldsymbol{x}^{gkso}_{best} - a_2. \times \boldsymbol{Xk}\right) + k_2\rho_{gkso}. \times (a_3. \times (\boldsymbol{X2} - \boldsymbol{X1})) + \frac{a_2}{2}. \times (\boldsymbol{Xu1} - \boldsymbol{Xu2}) \tag{82}$$

$$\boldsymbol{x}^{gkso}_{bin(i,:)} \leftarrow \boldsymbol{x}^{gkso}_{best} + k_1. \times \left(a_1. \times \boldsymbol{x}^{gkso}_{best} - a_2. \times \boldsymbol{Xk}\right) + k_2\rho_{gkso}. \times (a_3. \times (\boldsymbol{X2} - \boldsymbol{X1})) + \frac{a_2}{2}. \times (\boldsymbol{Xu1} - \boldsymbol{Xu2}) \tag{83}$$

Step 4 Convert the population $\boldsymbol{x}^{gkso}_{bin}$ from Step 3 to either zero or one by selecting the closest value between these two options, resulting in a binary population.

Step 5 Convert the binary population $\boldsymbol{x}^{gkso}_{bin}$ into an integer population, resulting in $\boldsymbol{x}^{gkso}_{int}$, with a structure similar to that in Equation (64).

Step 6 Limit the elements of the population $\boldsymbol{x}^{gkso}_{int}$ obtained in Step 5 to their corresponding bounds, as specified in Table 3.

Step 7 Evaluate the population from Step 6 using the training scenario set to obtain the corresponding objective function value (TNPC) for each agent. To do this, simulate the HPS considering the training scenario set and calculate the average TNPC ($TNPC^{avg}_{(\boldsymbol{a})}$) for each agent ($\boldsymbol{a}_{(i)}\ \forall\ i = 1,\ldots,I$) in the population.

Step 8 Compare the population obtained in Step 1 with that obtained in Step 6 regarding fitness (TNPC) and select the best agents. Sequentially compare each agent ($i = 1,\ldots,I$) from the population in Step 1 with the corresponding agent from the population

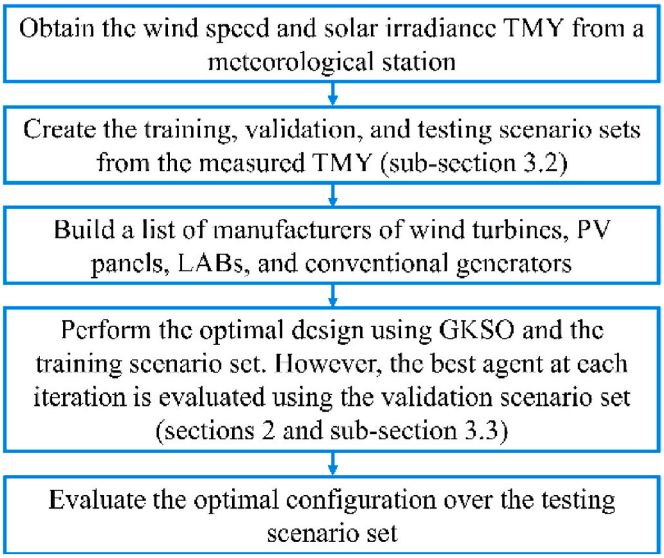

Fig. 6. Implementation of the proposed design methodology.

in Step 6, and select the option with the lowest TNPC. This results in the population obtained from the self-protection mechanism.

At each iteration ($k = 1, \dots, K$), the entire population is evaluated using the training scenario set, while only the agent with the best performance is evaluated using the validation scenario set. Once the optimization process has converged, we select the configuration with the lowest TNPC based on the evaluation of the validation dataset. This configuration is then evaluated over the testing scenario set for a more accurate performance analysis.

Regarding the problem constraints, if the condition of Equation (42) is not met, an arbitrarily high TNPC is assigned to the corresponding agent ($TNPC^{avg}_{(a)} \leftarrow \infty$), as this is a mandatory requirement. The constraints of Equations (44)–(46) are satisfied by the simulation model. On the other hand, the constraints of Equations (47)–(52) are addressed through penalty factors, which depend on how far the actual stress factors deviate from those specified in Table 4.

Using this approach, we allocate more computational resources to assessing the most promising agent through the validation scenario set, followed by a more accurate analysis at the end using the testing scenario set. The training scenario set allows us to explore the population with a reduced computational burden. Fig. 6 summarizes the optimization process introduced in this work for HPS design.

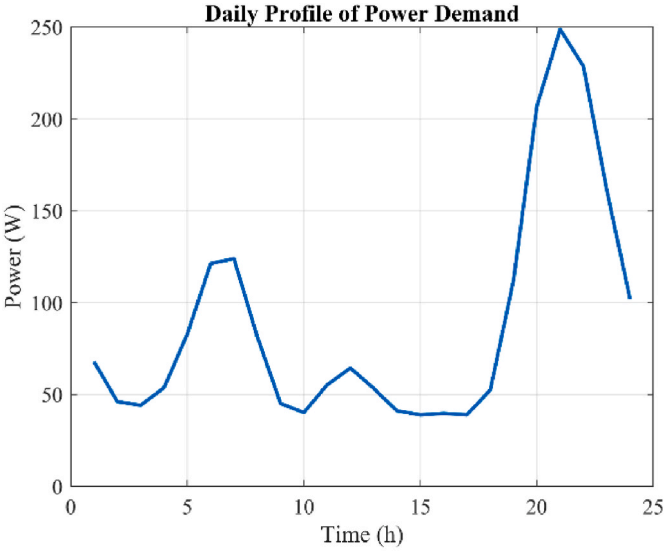

Fig. 7. Load demand profile.

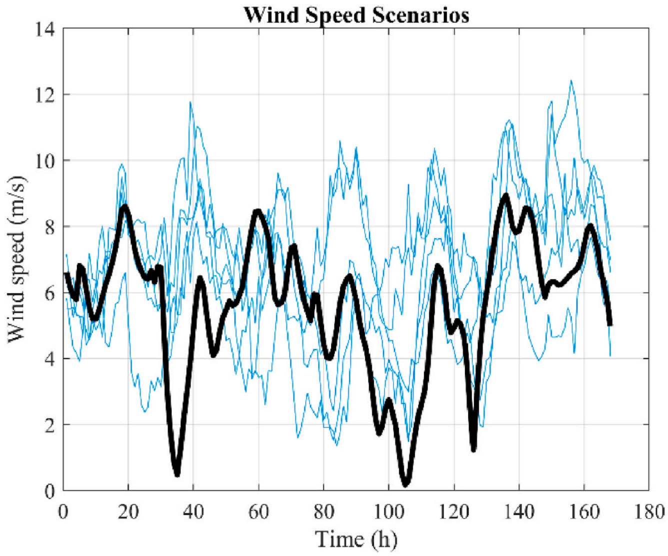

Fig. 8. First-week wind speed simulation (training scenario set).

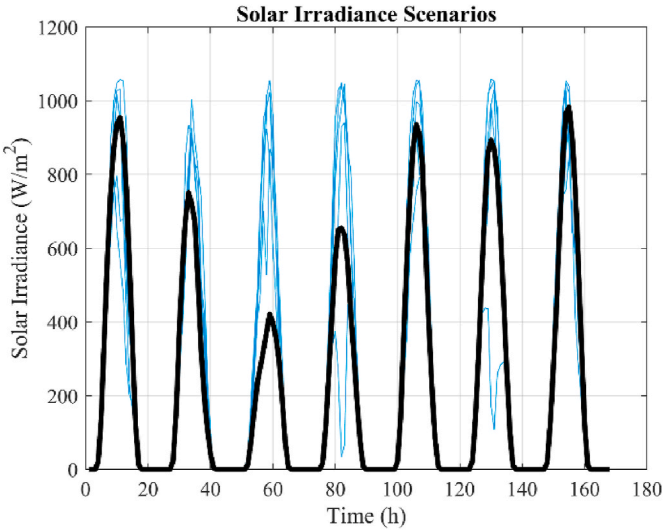

Fig. 9. First-week solar irradiance simulation (training scenario set).

The next section analyzes the proposed approach through the discussion of an illustrative case study.

4. Case study

The methodology introduced in this paper is illustrated through the design of an HPS located in Masvingo, Zimbabwe (latitude −20.7454°, longitude 31.3341°). The following sub-sections provide a detailed description and the results obtained.

4.1. Case study characteristics

The HPS is located in a remote area, with the power demand shown in Fig. 7. The daily profile was estimated by scaling the information available in Ref. [34] to a peak of 250 W. Additionally, the DC rating voltage was assumed to be 24 V. The proposed approach, including the simulation model described earlier, was implemented in MATLAB® on a PC equipped with an Intel Core® i7 CPU, 16 GB RAM, and a 64-bit operating system.

The procedure described in sub-section 3.2 was used to create the training, validation, and testing scenario sets. The time series length was 10 years with hourly intervals. Consequently, the training set consists of 5 scenarios, while both the validation and testing sets contain 25 scenarios each. These settings were chosen based on the available computational resources.

Figs. 8 and 9 present one week of wind speed and solar irradiance scenarios, along with the TMY obtained from Renewables.ninja [35–37].

We considered 30 wind turbine manufacturers with rated power ranging from 400 W to 7000 W and capital costs between 5002.021 € and 11752.67 €, respectively. O&M costs are estimated at 2 % of the capital costs on an annual basis.

Similarly, we considered 30 PV panel manufacturers. The rated power under STCs ranges from 50 W to 600 W, with capital costs between 68.97 € and 133.20 €, respectively. The average NOCT is 45.97 °C, and the temperature coefficient of power is -0.35 %/°C. The replacement cost was assumed to be equal to the capital cost, and O&M costs were neglected.

For the LABs, we also considered 30 manufacturers with rated capacities (C_{10}) ranging from 10 Ah to 3000 Ah, and capital costs ranging from 93.06 € to 470.398 €. The average number of cycles was 1087.8. The float lifetime was assumed to be 10 years for all manufacturers, and the minimum SOC was set at 30 %. The replacement cost was considered equal to the capital cost, and O&M costs were neglected.

Analogously, we considered 30 manufacturers of conventional gasoline-based thermal generators with power outputs ranging from 3000 W to 7000 W. Capital costs are estimated between 6356.732 € and 14930.732 €. The lifetime of all generators was estimated at 750 h, with O&M costs at 0.25 €/h. The parameters of the fuel consumption curve in Equation (39) were estimated using data from the manufacturers. The minimum operating power was assumed as 50 % of the rated value. The maximum number of PV panels, wind turbines, and LABs connected in parallel was set to 10. Finally, the economic parameters required for TNPC estimation are shown in Table 6.

The next sub-section presents and discusses the relevant results.

4.2. Result analysis and comments

The GKSO implementation, as previously described, was executed with 50 agents ($I = 50$) and a maximum of 100 iterations ($K = 100$). According to Table 3, the problem dimension is 7.

To save computational time, the optimization process was set to run for a minimum of 20 iterations. If the results did not change significantly during the last 10 iterations, the algorithm was stopped.

To avoid stagnation around a local optimum, GKSO was run 100 times using different seeds. The probability of finding a new local optimum in a single run of the optimization process was then estimated. This estimation was performed according to the method outlined in Ref. [38].

Fig. 10 shows the evolution of GKSO across each of the 100 experiments performed. It illustrates how the algorithm reaches different local optima. The solid line represents the evolution of the experiment that yielded the best results.

Fig. 11 presents the evolution of GKSO when the validation scenario set was evaluated. As previously explained, the solid line represents the evolution of the experiment that produced the best results.

Table 6
Economic indicators.

Inflation rate (%)	Nominal rate (%)	Project lifetime (year)	Gasoline price (€/liter)	Target EIU (%)
2.5	4.25	25	1.6	1

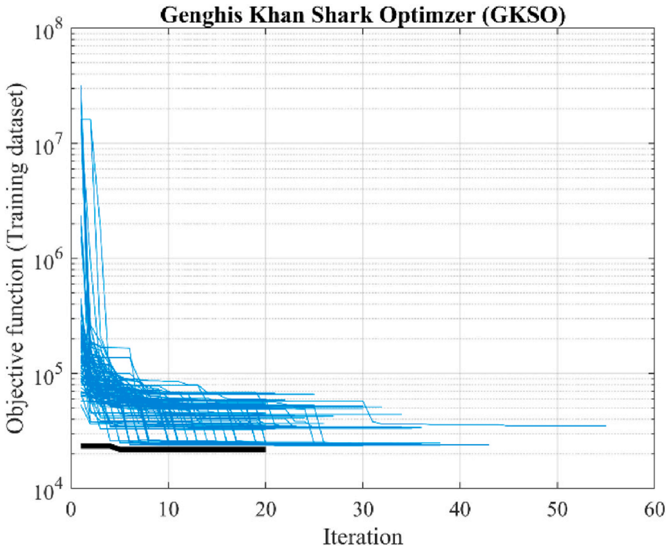

Fig. 10. Evolution of GKSO (training scenario set).

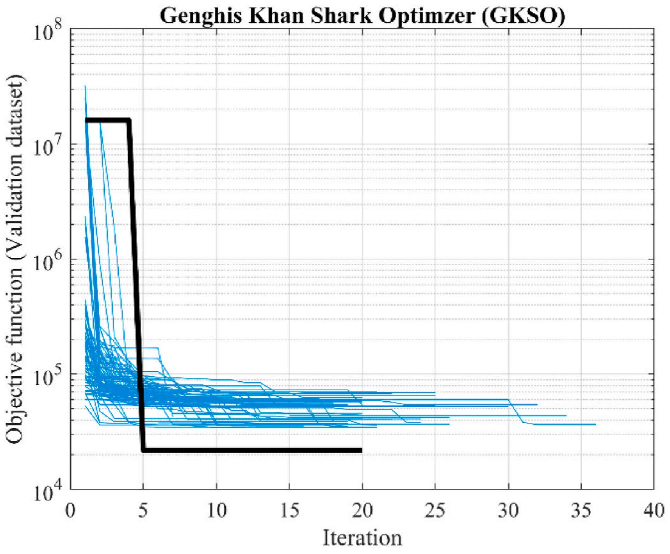

Fig. 11. Evolution of GKSO (validation scenario set).

It is important to note that the training set contains only 5 scenarios, while the validation set includes 25. When the algorithm settles around a local optimum, the best configuration may be feasible when considering the training set, but it might not be feasible when evaluated against the validation set, which is crucial for selecting the final solution. This explains why, when comparing Figs. 10 and 11, we observe fewer iterations corresponding to the validation set (Fig. 11). In other words, all solutions obtained after these few iterations were unfeasible.

By repeating the optimization process 100 times from different starting points, we search for different local optima—in other words, different configurations with their corresponding TNPC estimations. By analyzing the histogram of frequencies of the obtained TNPC estimations, we can assess the probability of having observed all local optima, or conversely, the probability of finding an unobserved local optimum if the optimization process is repeated once more. Details about this probabilistic estimation can be found in Ref. [35]. In this context, Fig. 12 shows the TNPC histogram, where each bin is assumed to represent a local optimum.

Based on the 100 experiments conducted and the information in

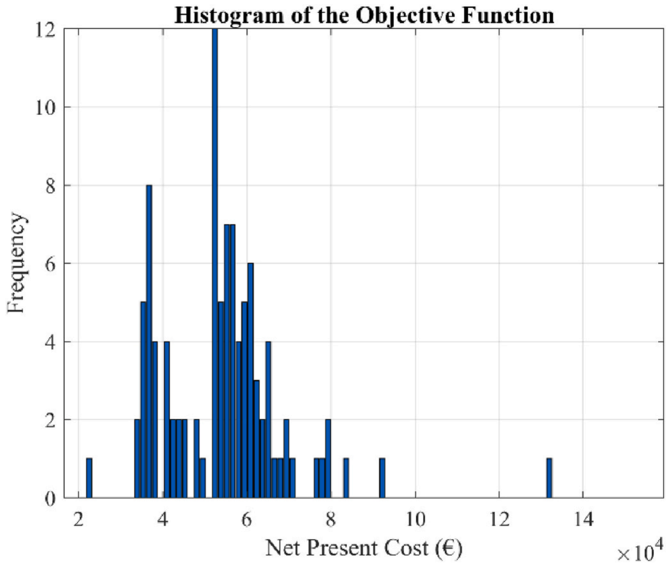

Fig. 12. Histogram of TNPC.

Table 7
Optimal HPS structure (GKSO).

Solar panel type (v)	Panels in parallel (d)	Wind turbine type (z)	Wind turbines (j)	Battery type (m)	Batteries in parallel (o)	Generator type (y)
1 (0 W)	9	3 (628 W)	1	8 (629 Ah)	1	1 (0 W)

Table 8
Economic performance of the optimal HPS (GKSO).

Total net present cost (€)	Energy index of unreliability (%)	Battery lifetime (year)
21988.96	0.44	3.91

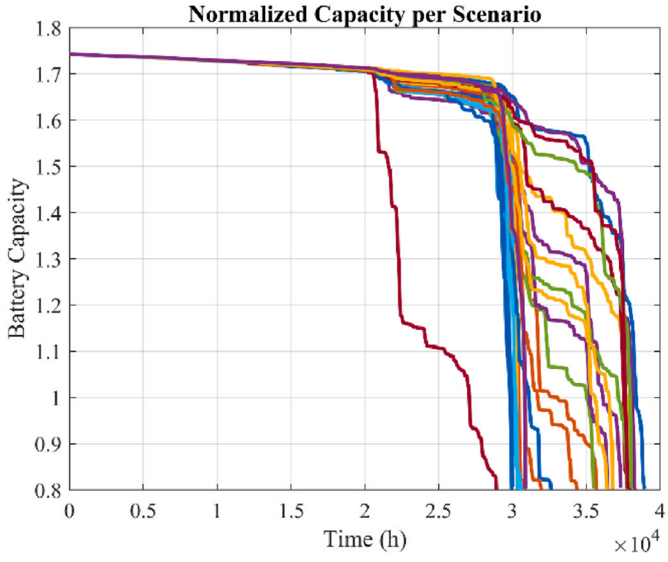

Fig. 13. BESS capacity.

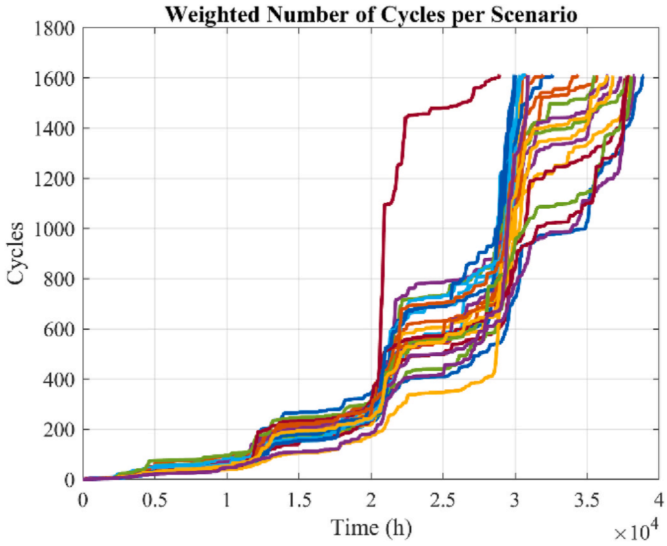

Fig. 14. BESS cycles.

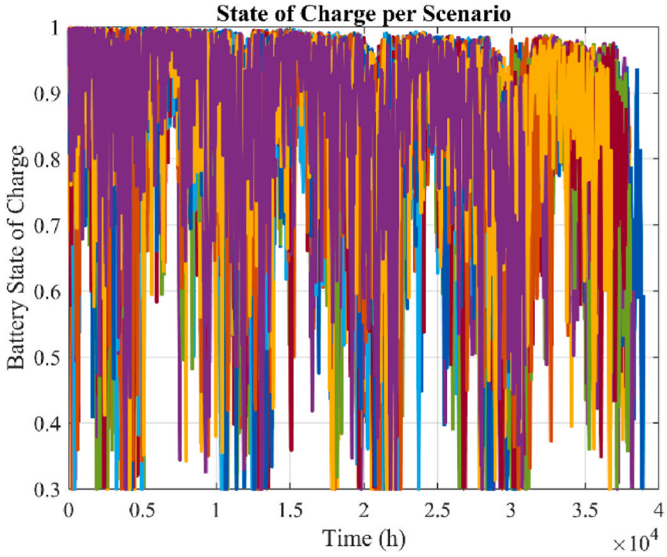

Fig. 15. Battery SOC.

Fig. 12, we estimated the probability of finding a new solution to be 0.11. The characteristics of the solution found are detailed in Tables 7 and 8. According to these results, only a wind turbine and a LAB battery are required. The expected battery lifetime is approximately 4 years.

Due to the importance of this component, Figs. 13–17 illustrate its expected performance in terms of capacity loss, cycles, SOC, voltage, and current.

Table 9 reports the operating stress factors related to the operation shown in Figs. 13–17. We observe that these factors satisfy the constraints of Equations (47)–(52), indicating operational similarities with an optimally designed SHS.

For comparative purposes, the optimal design problem was also solved using a GA with a population of 50 individuals over 100 generations, and crossover and mutation rates of 80 % and 10 %, respectively. During the optimization process, only the training scenario set was utilized. Once the final solution was identified, it was evaluated using the testing scenario set.

Tables 10 and 11 present the system's structure and performance. We observe that this configuration relies solely on wind and solar energy at their maximum capacities, without the inclusion of LABs or

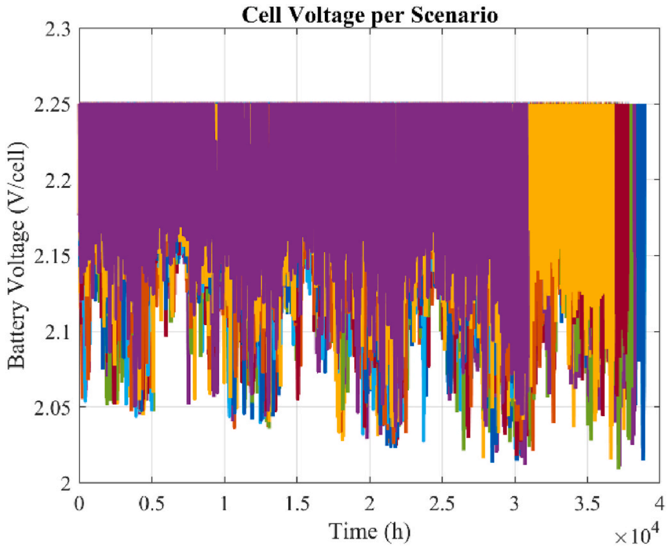

Fig. 16. Battery voltage.

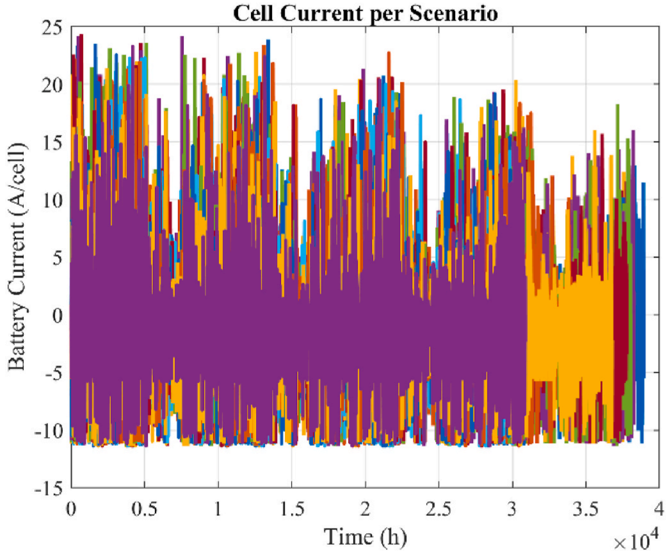

Fig. 17. Battery current.

Table 9
Target values for stress factors.

CF_{trg}	Q_{thr}^{trg}	$I_{1\%}^{max,trg}$	T_F^{trg}	PC_{trg}	T_S^{trg}
108.89	58.81	0.16	3.02	36.98	1.20

conventional generators. Additionally, we notice that the EIU is slightly higher than the target due to differences between the training and testing scenario sets. The training set contains only 5 scenarios, while the testing set includes 25, which is closer to a representative amount. Using the GA results (TNPC from Table 11) as a reference, the TNPC of the configuration obtained from the GKSO implementation (TNPC from Table 8) is 8.05 % lower. However, the computational time spent by GKSO in searching for the global optimum across 100 optimization processes is higher than that required by GA. This difference is evident in Table 12. The computational time could be reduced by leveraging cloud-based high-performance computing or by programming the available graphics processing unit to execute the 100 optimization processes concurrently, thereby decreasing the probability of identifying a new local optimum.

5. Conclusions and remarks

This paper presents a design methodology for HPS based on GKSO and illustrates it through a case study. The proposed methodology incorporates the variability of wind speed and solar irradiance, along with an advanced simulation model of the energy system. It includes both quantitative and qualitative perspectives through the weighted *Ah* throughput model and the assessment of battery stress factors, resulting in a comprehensive long-term evaluation of the system.

This simulation model is integrated into an optimization routine based on GKSO. Three scenario sets—one for training, one for validation, and one for testing—are used to account for the effects of resource variability. The training scenario set is used to evaluate the population during the optimization process, while the validation scenario set provides a reliable estimation of the performance of the best individual found at each iteration. The testing scenario set further refines the performance assessment of the optimal system configuration.

In the case study analyzed, the training set consisted of only 5 scenarios, while the validation and testing sets each contained 25. Using a training set with a limited number of scenarios helps reduce the computational burden, as this set is used to evaluate all agents in the population. Once the best agent is identified, it is evaluated using the validation set, which includes more scenarios and therefore provides greater precision. The testing set is an independent scenario group used to further enhance the performance analysis.

The global optimum was thoroughly searched by running the optimization process 100 times from different starting points. The probability of having observed all local optima was then estimated, resulting in 11 %. In other words, there is an 89 % probability that all the minima shown in Fig. 12 are the only existing ones. This provides valuable information about the optimality of the solution found.

Regarding the optimal configuration, GKSO suggested a wind-battery system, while the GA implementation resulted in a system utilizing solar and wind energy at their maximum capacities. The solution provided by GKSO was 8.05 % lower in TNPC compared to the one suggested by GA. These results demonstrate the promising capabilities of GKSO in handling combinatorial optimization problems.

A significant drawback of the proposed approach is its high

Table 11
Economic performance of the optimal HPS (GA).

Total net present cost (€)	Energy index of unreliability (%)
23913.73	1.07

Table 12
Comparison of computational time.

GKSO (hh:mm:ss)	GA (hh:mm:ss)
94:28:53	01:01:55

Table 10
Optimal HPS structure (GA).

Solar panel type (*v*)	Panels in parallel (*d*)	Wind turbine type (*z*)	Wind turbines (*j*)	Battery type (*m*)	Batteries in parallel (*o*)	Generator type (*y*)
31 (600 W)	2	31 (7000 W)	1	1 (0 Ah)	6	1 (0 W)

computational burden, primarily due to the exhaustive search for the global optimum. This issue could be mitigated by employing high-performance computing, which is readily accessible via cloud services. Alternatively, programming the graphics processing unit, commonly available in modern personal computers, offers another solution. Another key limitation of this research is the integration of DS characteristics associated with reducing PLs and VDs, both of which are critical in rural electrification projects. Regarding future research, incorporating additional storage technologies, such as lithium-ion or vanadium redox flow batteries, which have gained popularity in recent years, could further enhance the concepts presented in this study.

CRediT authorship contribution statement

Juan M. Lujano-Rojas: Conceptualization. **Rodolfo Dufo-López:** Funding acquisition. **Jesús Sergio Artal-Sevil:** Validation. **Eduardo García-Paricio:** Supervision.

Declaration of generative AI and AI-assisted technologies in the writing process

During the preparation of this work the authors used ChatGPT-4o in order to improve the language and readability of the manuscript. After using this service, the author reviewed and edited the content as needed and take full responsibility for the content of the publication.

Declaration of competing interest

The authors declare the following financial interests/personal relationships which may be considered as potential competing interestsRodolfo Dufo-Lopez reports financial support was provided by Spanish Government (Ministerio de Ciencia e Innovación, Agencia Estatal de Investigación). Rodolfo Dufo-Lopez reports financial support was provided by European Regional Development Fund. If there are other authors, they declare that they have no known competing financial interests or personal relationships that could have appeared to influence the work reported in this paper.

Acknowledgment

This work was supported by the Spanish Government (Ministerio de Ciencia e Innovación, Agencia Estatal de Investigación) and by the European Union/European Regional Development Fund [Grant PID2021-123172OB-I00 funded by MCIN/AEI/10.13039/501100011033 and by "ERDF A way of making Europe"]; [Grant TED2021-129801B-I00 funded by MCIN/AEI/10.13039/501100011033 and by European Union NextGenerationEU/PRTR].

Data availability

The data used is on the paper or available at the reported reference.

References

[1] Sadeghibakhtiar E, Naeimi A, Naderi S, Pignatta G, Behbahaninia A. Size optimization of a stand-alone solar-wind-battery hybrid system for net zero energy buildings: a case study. Energy Build 2024;313:114204. https://doi.org/10.1016/j.enbuild.2024.114204.

[2] Chen YJ, Zhang S. Technical, economic, and environmental assessment of a stand-alone power system based on diesel engine with/without energy storage using an optimization algorithm: a case study in China. Environ Sci Pollut Control Ser 2024. https://doi.org/10.1007/s11356-023-31488-3.

[3] Kamal MM, Asharaf I, Fernandez E. Optimal energy scheduling of a standalone rural microgrid for reliable power generation using renewable energy resources. Energy Sources Part A – Recovery Utilization and Environmental Effects 2023;45: 485–504. https://doi.org/10.1080/15567036.2023.2171511.

[4] Araoye TO, Ashigwuike EC, Mbunwe MJ, Bakinson OI, Ozue TI. Techno-economic modeling and optimal sizing of autonomous hybrid microgrid renewable energy system for rural electrification sustainability using HOMER and grasshopper optimization algorithm. Renew Energy 2024;229:120712. https://doi.org/10.1016/j.renene.2024.120712.

[5] Abdelsattar M, Mesalam A, Fawzi A, Hamdan I. Optimal design and analyzing the techno-economic-environmental viability for different configurations of an autonomous hybrid power system. Electrical Engineering 2024. https://doi.org/10.1007/s00202-024-02252-8. s00202-024-02252-8.

[6] Amoussou I, Paddy EY, Agajie TF, Ibrahim FS, Agajie EF, Nsanyuy WB, Bajaj M, Mohammadi SAD. Enhancing residential energy access with optimized stand-alone hybrid solar-diesel-battery systems in Buea, Cameroon. Sci Rep 2024;14:15543. https://doi.org/10.1038/s41598-024-66582-0.

[7] Bakeer A, Elmorshedy MF, Salama HS, Elkadeem MR, Almakhles DJ, Kotb KM. Optimal design and performance analysis of coastal microgrid using different optimization algorithms. Electrical Engineering 2023;105:4499–523. https://doi.org/10.1007/s00202-023-01954-9.

[8] Bouaouda A, Sayouti Y. An optimal sizing framework of a microgrid system with hydrogen storage considering component availability and system scalability by a novel approach based on quantum theory. J Energy Storage 2024;92:111894. https://doi.org/10.1016/j.est.2024.111894.

[9] Farh HMH. Neural network algorithm with reinforcement learning for microgrid techno-economic optimization. Mathematics 2024;12:280. https://doi.org/10.3390/math12020280.

[10] Jahangir DM, Syed IM, Meng Y, Davis B. Standalone hybrid PV/MHP/BES system sizing with complementarity adjustment. Int J Sustain Eng 2024;17:1–14. https://doi.org/10.1080/19397038.2024.2365190.

[11] Jiang JH, Ming B, Huang Q, Bai QJ. Operational robustness assessment of the hydro-based hybrid generation system under deep uncertainties. Energies 2024;17: 1974. https://doi.org/10.3390/en17081974.

[12] Yang S, Guo N, Zhang SM. Economic optimization of microgrid with demand response under source-load uncertainty. Energy Sources B Energy Econ Plann 2023;18:2280591. https://doi.org/10.1080/15567249.2023.2280591.

[13] Cheraghi R, Jahangir MH. Multi-objective optimization of a hybrid renewable energy system supplying a residential building using NSGA-II and MOPSO algorithms. Energy Convers Manag 2023;294:117515. https://doi.org/10.1016/j.enconman.2023.117515.

[14] Ansari AB. Multi-objective size optimization and economic analysis of a hydrogen-based standalone hybrid energy system for a health care center. Int J Hydrogen Energy 2024;62:1154–70. https://doi.org/10.1016/j.ijhydene.2024.03.165.

[15] Liu HT, Zhai RR, Patchigolla K, Turner P, Yu XH, Wang P. Multi-objective optimisation of a thermal-storage PV-CSP-wind hybrid power system in three operation modes. Energy 2023;284:129255. https://doi.org/10.1016/j.energy.2023.129255.

[16] Ahmed I, Rehan M, Basit A, Malik SH, Ahmed W, Hong KS. Adaptive salp swarm algorithm for sustainable economic and environmental dispatch under renewable energy sources. Renew Energy 2024;223:119944. https://doi.org/10.1016/j.renene.2024.119944.

[17] Belbachír N, Kamel S, Hassan MH, Zellagui M. Optimizing energy management of hybrid wind generation-battery energy storage units with long-term memory artificial hummingbird algorithm under daily load-source uncertainties in electrical networks. J Energy Storage 2024;78:110288. https://doi.org/10.1016/j.est.2023.110288.

[18] Mbasso WF, Naoussi SRD, Molu RJJ, Tsobze SK. Contribution into robust optimization of renewable energy sources: case study of a standalone hybrid renewable system in Cameroon. International Journal of Renewable Energy Research 2023;13:1093–118. https://doi.org/10.20508/ijrer.v13i3.14103.g8802.

[19] Hai T, Aksoy M, Faraji H. Techno-economic investigation of grid integrated renewable energy resources with hydrogen storage systems. J Energy Storage 2024;86:111248. https://doi.org/10.1016/j.est.2024.111248.

[20] Alahmad AK, Verayiah R, Shareef H. Long-term optimal planning for renewable based distributed generators and battery energy storage systems toward enhancement of green energy penetration. J Energy Storage 2024;90:111868. https://doi.org/10.1016/j.est.2024.111868.

[21] Alahmad AK, Verayiah R, Ramasamy A, Marsadek M, Shareef H. Optimal planning of energy storage system for hybrid power system considering multi correlated input stochastic variables. J Energy Storage 2024;82:110615. https://doi.org/10.1016/j.est.2024.110615.

[22] Pandya S, Jangir P, Trivedi IN. Multi-objective moth flame optimizer: a fundamental visions for wind power integrated optimal power flow with FACTS devices. Smart Science 2022;10:118–41. https://doi.org/10.1080/23080477.2021.1964693.

[23] Pandya SB, Kalita K, Jangir P, Cep R, Migdady H, Chohan JS, Abualigah L, Mallik S. Multi-objective RIME algorithm-based techno economic analysis for security constraints load dispatch and power flow including uncertainties model of hybrid power systems. Energy Rep 2024;11:4423–51. https://doi.org/10.1016/j.egyr.2024.04.016.

[24] Agrawal S, Pandya S, Jangir P, Kalita K, Chakraborty S. A multi-objective thermal exchange optimization model for solving optimal power flow problems in hybrid power systems, Decision Analytics. Journal 2023;8:100299. https://doi.org/10.1016/j.dajour.2023.100299.

[25] Xu W, Yu X. A multi-objective multi-verse optimizer algorithm to solve environmental and economic dispatch. Appl Soft Comput 2023;146:110650. https://doi.org/10.1016/j.asoc.2023.110650.

[26] Lambert T, Gilman P, Lilienthal P. Micropower system modeling with Homer. In: Farret FA, Godoy SM, editors. Integration of alternative sources of energy. Hoboken, New Jersey: John Wiley & Sons, Inc; 2006. p. 379–418.

[27] Schiffer J, Sauer DU, Bindner H, Cronin T, Lundsager P, Kaiser R. Model prediction for ranking lead-acid batteries according to expected lifetime in renewable energy

systems and autonomous power-supply systems. J Power Sources 2007;168:66–78. https://doi.org/10.1016/j.jpowsour.2006.11.092.
[28] Andersson A. Battery lifetime modelling. Denmark National Laboratory Risø; 2006.
[29] Bindner H, Cronin T, Lundsager P, Manwell JF, Abdulwahid U, Baring-Gould I. Lifetime modelling of lead acid batteries. Denmark National Laboratory Risø; 2005. https://www.osti.gov/etdeweb/servlets/purl/20607163.
[30] Svoboda V, Wenzl H, Kaiser R, Jossen A, Baring-Gould I, Manwell J, et al. Operating conditions of batteries in off-grid renewable energy systems. Sol Energy 2007;81:1409–25. https://doi.org/10.1016/j.solener.2006.12.009.
[31] Rampinelli GA, Krenzinger A, Romero FC. Mathematical models for efficiency of inverters used in grid connected photovoltaic systems. Renew Sustain Energy Rev 2014;34:578–87. https://doi.org/10.1016/j.rser.2014.03.047.
[32] Feijóo A, Villanueva D. Assessing wind speed simulation methods. Renew Sustain Energy Rev 2016;56:473–83. https://doi.org/10.1016/j.rser.2015.11.094.
[33] Hu G, Guo YX, Wei G, Abualigah L. Genghis Khan shark optimizer: a novel nature-inspired algorithm for engineering optimization. Adv Eng Inf 2023;58:102210. https://doi.org/10.1016/j.aei.2023.102210.
[34] Prinsloo G, Dobson R, Brent A. Scoping exercise to determine load profile archetype reference shapes for solar co-generation models in isolated off-grid rural African villages. J Energy South Afr 2016;27:11–27. https://doi.org/10.17159/2413-3051/2016/v27i3a1375.
[35] Renewables.ninja. https://www.renewables.ninja/. [Accessed 10 August 2024].
[36] Pfenninger S, Staffell I. Long-term patterns of European PV output using 30 years of validated hourly reanalysis and satellite data. Energy 2016;114:1251–65. https://doi.org/10.1016/j.energy.2016.08.060.
[37] Staffell I, Pfenninger S. Using bias-corrected reanalysis to simulate current and future wind power output. Energy 2016;114:1224–39. https://doi.org/10.1016/j.energy.2016.08.068.
[38] Finch SJ, Mendell NR, Thode HCJ. Probabilistic measures of adequacy of a numerical search for a global maximum. J Am Stat Assoc 1989;84:1020–3. https://www.jstor.org/stable/2290078.